

Searching for strong lensing by late-type galaxies in UNIONS

J. A. Acevedo Barroso¹, B. Clément^{1,2}, F. Courbin^{1,3,4}, R. Gavazzi^{5,6}, C. Lemon^{1,7}, K. Rojas^{8,9},
D. Scott¹⁰, S. Gwyn¹¹, F. Hammer¹², M. J. Hudson^{13,14,15}, and E. A. Magnier¹⁶

¹ Institute of Physics, Laboratory of Astrophysics, Ecole Polytechnique Fédérale de Lausanne (EPFL), Observatoire de Sauverny, 1290 Versoix, Switzerland

e-mail: javier.acevedobarroso@epfl.ch

² SCITAS, Ecole Polytechnique Fédérale de Lausanne (EPFL), 1015 Lausanne, Switzerland

³ Institut de Ciències del Cosmos (ICCUB), Universitat de Barcelona (IEEC-UB), Martí i Franquès 1, 08028 Barcelona, Spain

⁴ Institució Catalana de Recerca i Estudis Avançats (ICREA), Passeig de Lluís Companys 23, 08010 Barcelona, Spain

⁵ Laboratoire d'Astrophysique de Marseille, UMR7326, Aix-Marseille Université, CNRS, CNES, 13013 Marseille, France

⁶ Institut d'Astrophysique de Paris, UMR 7095, CNRS, and Sorbonne Université, 98 bis boulevard Arago, 75014 Paris, France

⁷ Oskar Klein Centre, Department of Physics, Stockholm University, SE-106 91 Stockholm, Sweden

⁸ University of Applied Sciences and Arts of Northwestern Switzerland, School of Engineering, 5210 Windisch, Switzerland

⁹ Institute of Cosmology and Gravitation, University of Portsmouth, Burnaby Rd, Portsmouth PO1 3FX, UK

¹⁰ Department of Physics and Astronomy, University of British Columbia, Vancouver, BC V6T 1Z1, Canada

¹¹ Canadian Astronomy Data Centre, Herzberg Astronomy and Astrophysics, National Research Council, 5071 West Saanich Rd Victoria BC V9E 2E7

¹² LIRA, Observatoire de Paris, Université PSL, CNRS, Place Jules Janssen 92195, Meudon, France

¹³ Department of Physics and Astronomy, University of Waterloo, Waterloo, ON, N2L 3G1, Canada

¹⁴ Waterloo Centre for Astrophysics, Waterloo, ON, N2L 3G1, Canada

¹⁵ Perimeter Institute for Theoretical Physics, 31 Caroline St. N., Waterloo, ON, N2L 2Y5, Canada

¹⁶ Institute for Astronomy, University of Hawaii, 2680 Woodlawn Drive, Honolulu, HI 96822, USA

Received September 15, 1996; accepted March 16, 1997

ABSTRACT

Recent wide-field galaxy surveys have led to an explosion in numbers of galaxy-scale strong gravitational lens candidates. However, the vast majority feature massive luminous red galaxies as the main deflectors, with late-type galaxies being vastly under-represented. This work presents a dedicated search for lensing by edge-on late-type galaxies in the Ultraviolet Near Infrared Optical Northern Survey (UNIONS). The search covers 3600 deg^2 of r -band observations taken from the Canada-France-Hawaii Telescope. We consider all sources with magnitudes in the range $17 < r < 20.5$, without any colour preselection, yielding a parent sample of seven million sources. We characterise our parent sample via the visual inspection of 120 000 sources selected at random. From it, we estimate, with a 68% confidence interval, that 1 in every 30 000 sources is an edge-on lens candidate, with at least eight high-quality candidates in the parent sample. This corresponds to 1 candidate per 17 000 edge-on late-type galaxies. Our search relies on a convolutional neural network (CNN) to select a reduced sample of candidates, followed by a visual inspection to curate the final sample. The CNN is trained from scratch using simulated r -band observations of edge-on lenses, and real observations of non-lenses. We find 61 good edge-on lens candidates using the CNN. Moreover, combining the CNN candidates with those found serendipitously, and those identified while characterising the parent sample, we discovered 4 grade A, 20 grade B, and 58 grade C edge-on lens candidates; effectively doubling the known sample of these systems. We also discovered 16 grade A, 16 grade B, and 18 grade C lens candidates of other types. Finally, based on the characterisation of the parent sample, we estimate that our search found around 60% of the bright grade A and B edge-on lens candidates within the parent sample.

Key words. Gravitational lensing: strong – Galaxies: spiral – Methods: data analysis – Methods: observational

1. Introduction

Strong gravitational lensing has become an essential tool for probing the extragalactic Universe. Its applications range from the detection and study of high-redshift sources (e.g., Atek et al. 2023; Bradley et al. 2023), including the mapping of the mass distributions responsible for the lensing effect (e.g., Shajib et al. 2019; Etherington et al. 2022; Mahler et al. 2023), to the constraining of cosmological parameters, most notably H_0 when the lensed source exhibits time variability (e.g., Wong et al. 2020; Birrer et al. 2020; Kelly et al. 2023; Chen et al. 2024). Additionally, the analysis of flux ratios be-

tween multiply-lensed images, alongside small-scale distortions in the lensed arcs, allows for the detection of mass clumps in the line of sight (e.g., Vegetti et al. 2010; Nightingale et al. 2023; Nierenberg et al. 2024; Gilman et al. 2024; Nightingale et al. 2024). Furthermore, combining lens modelling with a second probe of mass can break degeneracies in our mass models that limit the individual analyses, such as the baryonic and dark matter degeneracy (e.g., Auger et al. 2010; Schuldt et al. 2019; Sheu et al. 2024), the bulge-disc degeneracy for late-type galaxies (e.g., Dutton et al. 2011; Suyu et al. 2012), or the mass-sheet degeneracy, which affects lens models in general (e.g., Shajib et al. 2023; Khadka et al. 2024). In particular, galaxy-scale lensing, when combined with deep spectro-

* e-mail: javier.acevedobarroso@epfl.ch

scopic observations or multi-band photometry, can probe the stellar initial mass function (IMF) of the lensing galaxies, see Ferreras et al. (2010); Czoske et al. (2012); Dutton & Treu (2014); Brewer et al. (2014); Sonnenfeld et al. (2019).

However, these studies are limited by their sample size, and their results can change with improved samples and statistics. This is especially the case for late-type galaxies, for which the sample of confirmed lenses is in the few tens. Whether the IMF is the same for late-type galaxies as it is for early-type, in what way the IMF might differ in the bulge from the disc for a given galaxy, and the universality of the IMF for late-type galaxies, are all open questions that can be tackled with large samples of late-type lens galaxies. In this context, the Sloan WFC Edge-on Late-type Lens Survey (SWELLS; WFC – wide field camera) launched a campaign in the early 2010 decade to find and study lensing by edge-on late-type galaxies (edge-on lenses), while trying to answer the aforementioned questions. This series of six papers includes: the curation and characterisation of a spectroscopically selected sample of edge-on lenses (Treu et al. 2011); the combination of lens modelling with spatially-resolved kinematics to break the disc-halo degeneracy and probe the IMF for a single galaxy (Dutton et al. 2011; Barnabè et al. 2012); the systematic comparison between the total mass inside the Einstein radius and the stellar mass estimated from stellar population synthesis (SPS) models to study the IMF for medium-sized samples (≈ 20) of edge-on lenses (Brewer et al. 2012, 2014); and the study of the IMF normalisation of the bulge and the disc independently for a sample of five edge-on lenses using lens modelling, kinematics, and SPS (Dutton et al. 2013). To date, the SWELLS papers represent the largest study of edge-on lenses, but it is still limited to a couple tens of systems.

Moreover, galaxy-scale strong lensing events are very rare. The likelihood of observing these events depends on the mass distribution of the deflectors and the redshift distributions of foreground lenses and background sources. As a result, only about one source in thousands exhibits lensed images (e.g., Oguri & Marshall 2010; Collett 2015; Ferrami & Wyithe 2024; Acevedo Barroso et al. 2024), and those are not easy to see in ground-based imaging, both because of the small image separation on the plane of the sky and because of the low luminosity contrast between the lens light and the background source. This is true when the lens galaxy is a massive luminous red galaxy (LRG), but the situation is even worse for the less massive late-type galaxies. In fact, only about a hundred lens candidates have a late-type deflector, out of approximately twenty thousand lens candidates known by the community (see Vernardos et al., in prep.). More so, even though the number of lens candidates is growing orders of magnitude faster since the adoption of machine learning in lens finding, the number of late-type candidates has been growing at a much more modest rate, hinting at the necessity of lens searches that target them directly.

Recent massive optical lens searches are targeting wide-sky surveys to maximise the volume probed, while also using neural networks to select samples of potential lens candidates. These surveys include the Dark Energy Survey (DES; Jacobs et al. 2019a,b; Rojas et al. 2022; O’Donnell et al. 2022), the Kilo-Degree Survey (KiDS; Pettillo et al. 2017, 2019; He et al. 2020; Li et al. 2020, 2021), the Subaru Hyper Suprime-Cam (HSC; Cañameras et al. 2021; Shu et al. 2022; Jaelani et al. 2024; Schuldt et al. 2025), the Dark Energy Spectroscopic Instrument (DESI) Legacy Imaging Survey (Huang et al. 2020, 2021; Stein et al. 2022; Storfer et al. 2024), the *Euclid* Early Release Observations (Nagam et al. 2025), and the Ultraviolet Near Infrared Optical Northern Survey (UNIONS; Savary et al.

2022). Most of the analyses rely on convolutional neural networks (CNNs) as the main classifier, but visual transformers are also being explored as an alternative (Grespan et al. 2024; González et al. 2025).

Given the extremely low prevalence of lensing events, it is common to restrict lens searches to the most massive galaxies, often making a colour preselection for LRGs. These preselections remove most of the late-type galaxy lenses, excluding them from the lens search even before the CNNs inspect them. However, even if there is no colour preselection, there are still not enough confirmed lenses to train neural networks using only real observations. Instead, the CNNs are trained on mock observations simulating the lensing effect. These mock lenses are being refined, from the first ones by Pettillo et al. (2017), randomly adding fully simulated lensed sources to LRGs, to the recent use of real deep *HST* observations for the potential sources, and the dynamics of the potential deflectors to select a reasonable lensing mass (Cañameras et al. 2020; Rojas et al. 2022; Savary et al. 2022). The problem with this methodology is that it limits the search to the lens candidates that look the most similar to the mock lenses used to train the networks. And, since these studies mostly use LRGs for the deflector galaxies, then late-type lenses are also indirectly excluded, even if they are part of the parent sample inspected by the networks.

Another limitation in the discovery of late-type galaxy lenses is their relatively lower mass compared to early-type galaxies. This, combined with the characteristic bulge-disc morphology of late-type galaxies, results in most of the lensing being caused by the bulge when the galaxy is not viewed edge-on. In such cases, the Einstein radius is often too small to be resolved by most ground-based surveys. Consequently, it is expected that most late-type galaxy lenses detectable by ground-based surveys will have an edge-on orientation.

In this work, we search for galaxy-scale lensing by late-type edge-on disc galaxies (hereafter ‘edge-on lenses’) in the Canada-France Imaging Survey (CFIS), now a part of UNIONS. We choose this survey because of its excellent image quality, large area coverage, and its complete overlap with the on-going Euclid Wide Survey (Euclid Collaboration: Scaramella et al. 2022; Euclid Collaboration: Mellier et al. 2024). This represents the second lens search specifically targeting edge-on lenses in optical data, after Sygnet et al. (2010), who also used data from the Canada-France-Hawaii Telescope (CFHT). However, this is the first time it is being done using machine learning and the methodology popularised in the last decade. Our main objective is to substantially increase the sample of known edge-on lens candidates, while also exploring why they are not being found by the recent massive lens searches. Additionally, we aim to estimate the prevalence and total number of edge-on lenses in the data, and develop a framework to evaluate the performance of our CNN-search without relying on simulated lenses.

This paper is organised as follows. We present the UNIONS-CFIS observations and the selection of the parent sample in Sect. 2. Then, in Sect. 3, we characterise the parent sample by estimating the number of lenses in it. We describe the process to simulate mock observations of edge-on lenses in Sect. 4, and present the training and deployment of the CNN in Sect. 5. We present spectroscopic follow-up of two candidates from the Nordic Optical Telescope (NOT) in Sect. 6. Finally, we discuss our findings and conclude in Sects. 7 and 8, respectively.

2. Data

We use r -band data from CFIS data release 3, conducted using the 3.6-m CFHT on Maunakea, Hawaii. CFIS provides deep r - and u -band imaging to UNIONS, a collaboration of wide-field imaging surveys of the northern sky involving CFIS, as well as members of the Panoramic Survey Telescope And Rapid Response System (Pan-STARRS) team, the Waterloo Hawaii Institute for Astronomy G-band Survey (WHIGS) team, and the Wide Imaging with Subaru Hyper Suprime-Cam of the Euclid Sky (WISHES) team. Deep i -band and moderately deep z -band imaging data are provided by Pan-STARRS, deep g -band data are provided by WHIGS, and deep z -band data are provided by the WISHES team. UNIONS aims to provide ground-based complementary data for the *Euclid* mission, as well as maximising the science output of these ground-based large-area deep imaging surveys (Ibata et al. 2017; Guinot et al. 2022).

The CFIS data release 3 covers 7000 deg² down to a median depth of 24.3 in the u -band, and 3600 deg² down to a median depth of 25.2 in the r -band. Both depths are for point sources with 5σ detection in a 2'' aperture. The median seeing of the data is 0''.8 and 0''.6 for the u - and r - bands, respectively. The individual observations were reduced, calibrated and co-added at the Canadian Astronomy Data Centre (CADC) using a modified version of the MegaPipe pipeline (Gwyn 2008, 2019). The final images have a pixel size of 0''.1857. Additionally, models of the point spread function (PSF) and its spatial variations were produced for every co-added frame using PSFEx (Bertin 2011). In the present work, we focus on CFIS r -band data due to their exquisite seeing quality. This is crucial for our specific search, since late-type edge-on galaxies have a smaller lensing cross-section than the typical LRGs used in other searches. As a consequence, the potential lensed images are more often hidden in the glare of the lens light than for systems with early-type lens galaxies.

We classify detections with flux radius larger than one standard deviation above the median value as extended sources. We then extract postage stamps of 66 × 66 pixels (12''.256 × 12''.256) for every extended source within the range 17.0 < r < 20.5, amounting to 6 978 977 stamps. For each source, we also use an RMS map and a PSF image generated from the PSFEx model and oversampled by a factor of 2. This is our ‘parent sample’, which is further characterised in Sect. 3.

3. Estimating the number of lenses in the parent sample

3.1. The challenges of finding rare objects

We approach the lens search as a binary image classification problem, where the target class is composed of stamps displaying reasonable lensing features. To tackle this problem, we use a supervised machine-learning approach, training our CNN on a set of correctly classified images. The goal is that, upon encountering a new image, the network will correctly classify it based on the patterns learned from the training data. While this approach is standard practice in image classification, the extremely low prevalence of edge-on lenses on the sky presents additional challenges.

The first challenge is that there are not enough observations of edge-on lenses to train a CNN from scratch, which requires tens of thousands of examples, while only about a hundred edge-on lens candidates are currently known. Consequently, we have to produce a simulated training set for the network. It remains

an open question how much the use of simulations affects the precision and completeness of the lens search.

The second challenge resides in a combination of networks producing false positives and having to face the so-called ‘base rate fallacy’: even if the network correctly classifies non-lenses most of the time, for example 99.9% of the sample, the remaining misclassified 0.1% is still large enough to dominate the sample of lens candidates suggested by the network. This is best illustrated using the Bayes’ rule, stating that

$$P(L|C) = \frac{P(C|L)P(L)}{P(C)}, \quad (1)$$

where $P(L|C)$ is the probability that something classified as a lens candidate is indeed a lens, this represents the ratio of lenses over machine-selected candidates, and is often called the ‘purity’ of the lens search. On the other hand, $P(C|L)$ is the probability that the CNN correctly classifies the image of a lens as a lens. This is also known as the true positive rate (TPR), or recall. $P(L)$ is the probability of a random stamp being a lens, which is the prevalence of lensing on the sky. $P(C)$ is the probability that the CNN classifies any given stamp as a lens. Since every stamp shows either a lens or not, we marginalise the last term as

$$P(C) = P(C|L)P(L) + P(C|\text{Non-L})(1 - P(L)), \quad (2)$$

with $P(C|\text{Non-L})$ being the probability that the network mistakenly classifies an image that does not contain any lensing features as a lens. This is known as the false positive rate (FPR). Equation (1) becomes

$$P(L|C) = \frac{P(C|L)P(L)}{P(C|L)P(L) + P(C|\text{Non-L})(1 - P(L))}. \quad (3)$$

Taking the conservative estimate that one object shows lensing features for every 10 000 galaxies, then $P(L) = 10^{-4}$. If we further assume a network capable of correctly classifying all lenses in a sample and 99% of the non-lenses, then $P(C|L) = 1$ and $P(C|\text{Non-L}) = 0.01$. From there, Eq. (3) implies that only 1% of the stamps classified as lenses by the network are in fact real lenses, that is, $P(L|C) \approx 0.01$.

The latter point is probably the main limitation of automated lens finding approaches in general, because it challenges even the very best networks currently available. Moreover, this is further complicated by the fact that many objects that have nothing to do with lensing do display morphological structures that efficiently mimic lensing. This is the third challenge to face. An immediate consequence of all the above is that even when using the best techniques, a final visual inspection step is needed to compile a reliable list of lens candidates.

3.2. The visual inspection

To estimate the number of galaxy-scale lenses in the parent sample, we conduct a systematic visual inspection of randomly selected sources. This procedure allows us to establish a baseline against which we can compare the performance of our CNN classifier. Additionally, it provides some estimates of the potential of the parent sample for future, more general, lens finding efforts. For this, we split the parent sample into four r -band bins of magnitude (17, 18], (18, 19], (19, 20], and (20, 20.5]. We then randomly select 30 000 sources per bin to be inspected, for a total of 120 000 sources probed. A similar procedure is used in Acevedo Barroso et al. (2024) to estimate the number of lens candidates in the entire Euclid Wide Survey.

For the visual inspection, we follow a three-step methodology, in which the sources selected in one step go on to be reinspected in the next one:

- Step 1: the experts individually inspect the sources in mosaics;
- Step 2: the experts individually inspect the sources one at a time;
- Step 3: the experts collectively inspect the sources one at the time.

For this purpose, we have reimplemented the visualisation tools used in Rojas et al. (2022) and Savary et al. (2022) using the Qt6 framework.¹ The tools correspond to a mosaic viewer that shows multiple sources in a rectangular grid, and a 1-by-1 sequential tool that displays a single source at a time. Both tools allow the user to change the colour-map and scaling function used to display the stamps. The mosaic tool is used for binary classification: the user goes through pages of mosaics and clicks on the stamps that show hints of lensing. By contrast, the 1-by-1 sequential tool allows for the detailed classification of sources into the following non-overlapping categories:

- A, shows clear lensing features and no additional information is needed;
- B, shows lensing features but additional information is required to confirm its lensing nature;
- C, shows lensing features, but these can be explained by other phenomena;
- X, definitively not a lens.

Additionally, the 1-by-1 sequential tool offers quick access to three *grz* colour-composite images from the DESI Legacy Imaging Survey (Dey et al. 2019, Legacy Survey henceforth): a colour-composite image covering the area of the stamp inspected ($12''.256 \times 12''.256$); a colour-composite image displaying the environment around the stamp in a larger field of view ($2'.13 \times 2'.13$); and a colour-composite covering the same area as the stamp, but displaying the residuals of the inference modelling used to construct the DESI source catalogue. We present an example of the two tools in Fig. 1, for which the 1-by-1 sequential tool is showing the environment around the inspected stamp.

The first two steps of the visual inspection were performed by J.A.A.B., B.C., and F.C. Each one inspected a different set of 10 000 sources from each of the magnitude bins during the mosaic step. Then, all the candidates selected by any of the three human classifiers were pooled together for the individual 1-by-1 inspection. Lastly, the final group inspection was done by six expert classifiers J.A.A.B., B.C., F.C., C.L., R.G., and K.R. During the final inspection, the classifiers had access to *r*- and *u*-band UNIONS imaging, as well as the Legacy Survey data previously described. They also used, when available, *grizy* imaging data from Pan-STARRS (Chambers et al. 2016; Flewelling et al. 2020), and spectral data from the Sloan Digital Sky Survey (SDSS; Blanton et al. 2017).

The visual inspection rendered eight grade A, six grade B, and 23 grade C candidates. This includes one grade B edge-on lens candidate and nine grade C. The candidates are displayed in Fig. 2.

3.3. Extrapolating to the whole parent sample

We use Bayes' theorem to estimate the number of lens candidates in the parent sample from the number of candidates found

¹ Available at <https://github.com/ClarkGuilty/Qt-stamp-visualizer>.

in the visual inspection. To do so, we make the following assumptions:

1. we have identified all the lenses in the sample probed (30 000 per magnitude bin);
2. being randomly selected, the sample probed is representative of the entire parent sample.

Under these assumptions, the likelihood $P(k|K)$ of finding k lens candidates in the probed sample out of a parent sample containing K lens candidates is given by

$$P(k|K) = \frac{\binom{K}{k} \binom{N-K}{n-k}}{\binom{N}{n}}, \quad (4)$$

where n is the number of sources probed and N is the number of sources in the parent sample. Then, we estimate $P(K|k)$: the posterior probability that there are K lenses in the parent sample, given that we have found k in the sample probed. Following Bayes' theorem: $P(K|k) \propto P(k|K)P(K)$. Last, we institute a prior on the number of lenses in the parent sample $P(K)$, such that the probability of a random source showing lensing features (K/N) is distributed uniformly logarithmically between 10^{-10} and unity.

We make the calculation independently for every magnitude bin, but join the grades A and B to increase the signal. The results are summarised in Table 1. We further classify 10 of the candidates as edge-on based on the morphology of their deflector galaxy. However, only one of them is deemed grade A, while the rest are deemed grade C. This good candidate belongs in the brightest magnitude bin, hinting at a core problem of searching for edge-on lenses: the lensed light is very often blended with the deflector, leading to uncertain classifications. The low signal in our measurement means that the estimates are prior-dominated for all the other magnitude bins and correspond only to upper bounds. Overall, we estimate at least eight grade A and B edge-on lens candidates, and at least 500 candidates for lensing in general. This is consistent with a prevalence rate of 1 lens for every 10 000 sources for lensing in general, and 1 in 30 000 for edge-on lenses.

4. Simulating a training data set

We use the data-driven methodology introduced by Cañameras et al. (2020) and reproduced by Rojas et al. (2022) and Savary et al. (2022) to produce a large data set of simulated lenses to train our CNN. This requires us to select a set of real UNIONS sources as potential deflector galaxies. For each deflector, we assume a composite mass model comprising both a baryonic component and a dark matter halo. We then simulate the lensing of real galaxies from deep *HST* imaging data, and add the resulting arcs on the UNIONS images of our selection of deflectors. We use the same *HST* sources with HSC colours described in Rojas et al. (2022). For all the lensing calculations and image simulations we use the Python package Lenstronomy (Birrer & Amara 2018; Birrer et al. 2021), and we use Astropy (Astropy Collaboration et al. 2022) to handle the imaging data. Figure 3 gives a visual summary of the complete simulation algorithm. We describe below the different elements of the process.

4.1. Selection of potential CFIS deflectors

We begin the process by selecting the edge-on late-type galaxies in our CFIS data. To do so, we apply an ellipticity cut similar

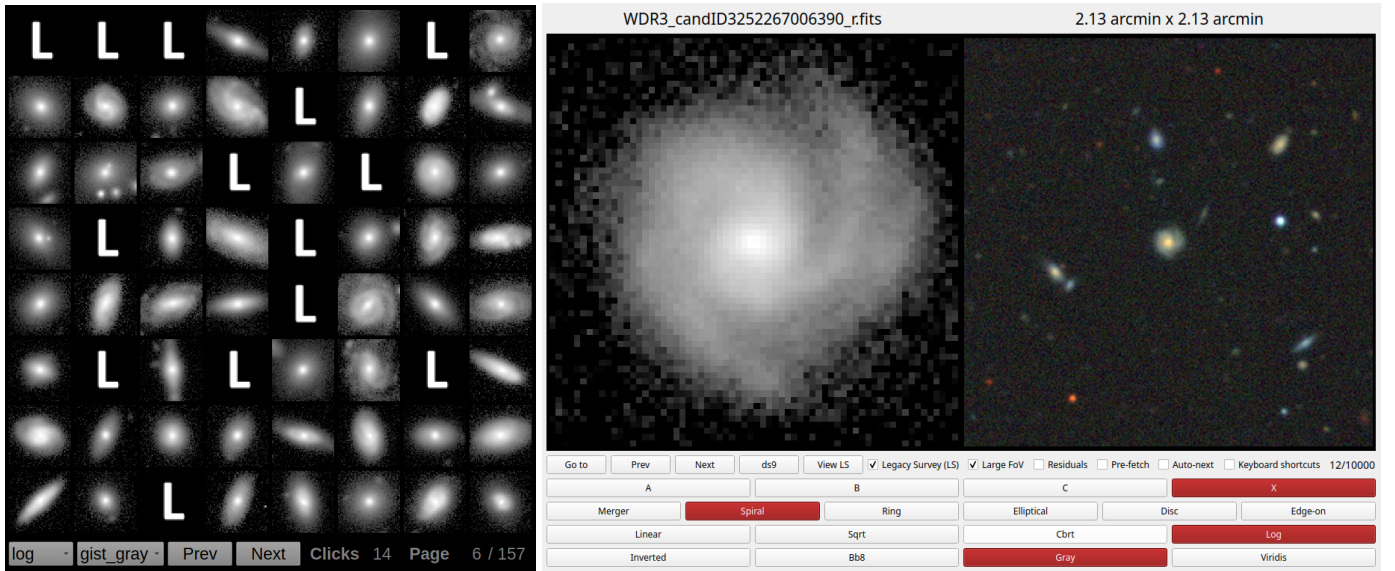


Fig. 1. Visualisation tools used for the visual inspections. *Left panel:* the mosaic tool showing an 8×8 grid, whilst highlighting sources classified as ‘lenses’ with a capitalised ‘L’ instead of the UNIONS stamp. *Right panel:* The 1-by-1 sequential tool showing a spiral galaxy on the left side, and the larger field of view from Legacy Survey on the right side. The source is classified as a ‘non-lens’ and further sub-classified as a ‘spiral’. Both applications are using logarithmic scale and a grey colour-map for the UNIONS stamps.

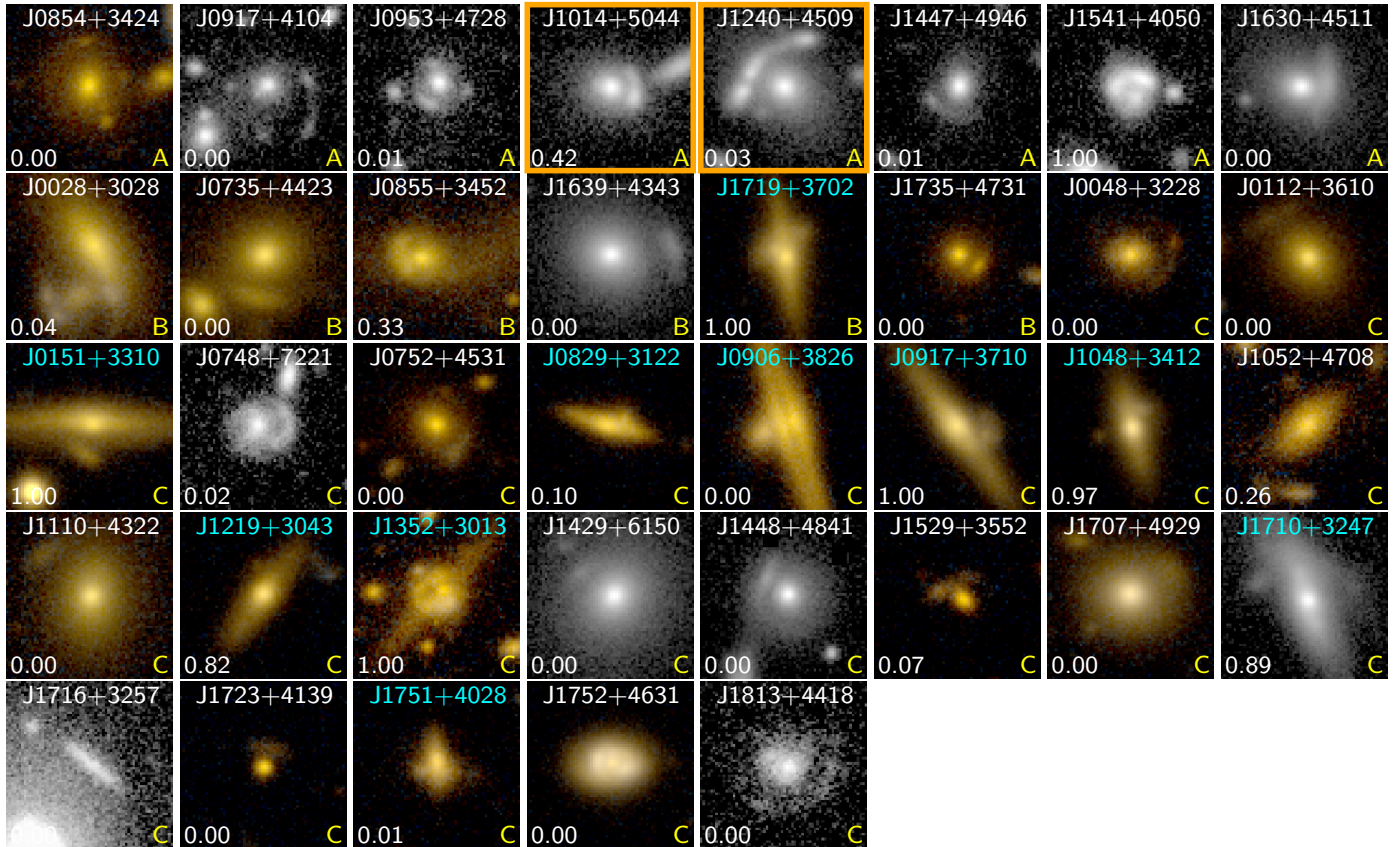


Fig. 2. Lens candidates discovered during the prevalence study, sorted by visual inspection grade and right ascension. We show a colour composite of the r - and u -bands when u -band data are available, otherwise we just display a grey-scale r -band image. The number in the bottom left is the CNN score, and the letter in the bottom right corresponds to the final human classification. We highlight the edge-on lenses with their name in cyan, and the candidates previously reported in the Strong Lens Database (SLED) with an overlaid orange square.

to the one used by Sygnet et al. (2010), namely $0.6 < e < 0.92$, with

$$e \equiv \frac{a^2 - b^2}{a^2 + b^2}, \quad (5)$$

where a and b are the semi-major and semi-minor axes of the light distribution, respectively. The lower limit on the ellipticity removes most of the non-edge-on galaxies while the upper limit removes artefacts such as dead columns, stellar spikes, fast aster-

Table 1. Estimate of the number of lens candidates in the parent sample. This is derived from the expert visual inspection of $n = 30\,000$ randomly selected sources per magnitude bin. Uncertainties are given for a 68% confidence interval. Results are shown for both strong lensing in general, and for edge-on lenses only. If no candidates were found, the estimation corresponds to a prior-dominated upper bound. The names of the columns in parenthesis match the elements of Eq. (4).

Grade	Mag. bin	Population size (N)	Edge-on deflector		Any deflector	
			Counts (k)	Expected total (K)	Counts (k)	Expected total (K)
A+B	17 to 18	328 345	1	11 [8, 35]	5	55 [40, 90]
A+B	18 to 19	999 184	0	< 37	3	100 [70, 195]
A+B	19 to 20	2 848 367	0	< 108	4	380 [271, 677]
A+B	20 to 20.5	2 802 381	0	< 106	2	187 [129, 431]
C	17 to 18	328 345	5	55 [40, 90]	11	120 [95, 166]
C	18 to 19	999 184	3	100 [70, 195]	6	200 [148, 317]
C	19 to 20	2 848 367	1	95 [68, 311]	2	190 [131, 438]
C	20 to 20.5	2 802 381	0	< 106	4	374 [267, 666]

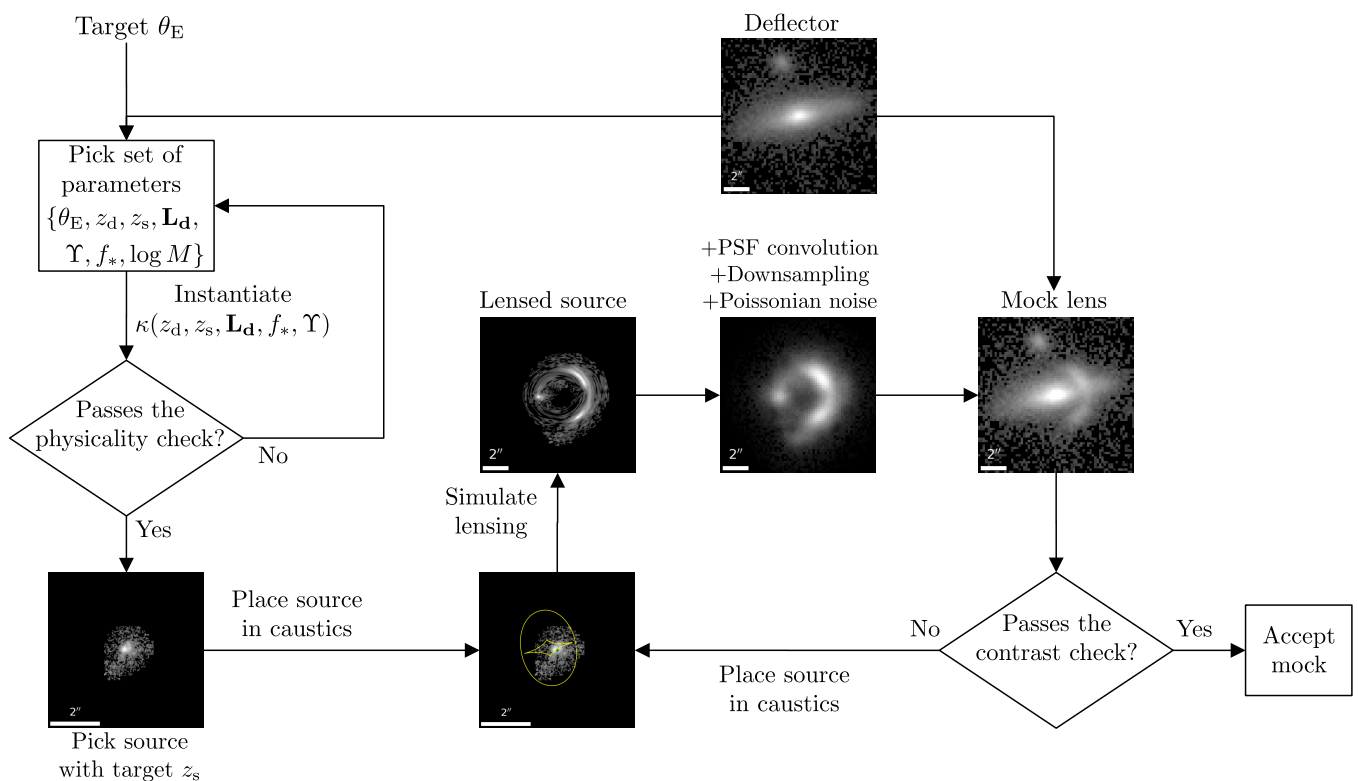


Fig. 3. Schematic description of our lens simulation procedure. To produce each simulated stamp, we start with a potential deflector and a target Einstein radius, θ_E . Then, we pick a set of parameters for a mass model consistent with the target θ_E and the deflector’s light, and perform a check where we make sure that $\log M$, f_* , and Υ are within physical ranges. After that, we pick a source using the target z_s provided by the mass model parameters, and place it randomly around the caustics before simulating its lensing by the mass model. Next, we convolve the lensed source image with the deflector’s PSF, then downsample to match the pixel size of CFIS, and add Poissonian noise. At this point, we add the original stamp of the deflector to get the final mock. Lastly, we perform a contrast check to make sure that the lensing features are visible. If it passes the check, we accept the mock and proceed to the next deflector. Otherwise, we reposition the source relative to the caustics and try a second time.

oids or any other spurious objects with extreme ellipticities. Due to PSF smearing, the percentage of selected galaxies decreases with magnitude, from 18% for the brightest galaxies ($r = 17$) to 12% for the faintest ($r = 20.5$).

Then, we cross-match the selected galaxies with SDSS data release 17 (Abdurro’uf et al. 2022) to obtain photometric redshifts (photo- z), K-corrections, and distance moduli. We keep only those galaxies with `photoErrorClass = 1` in the SDSS catalogue, ensuring the best possible estimation of the photo- z error. We note that the SDSS data do not cover the entire CFIS footprint; however, this is not a problem as long as there are

enough galaxies with photo- z to build a training data set. On the other hand, the photo- z error increases with magnitude, such that it is about 6 times larger for the faintest galaxies ($\Delta z \approx 0.13$) than for the brightest ones ($\Delta z \approx 0.02$). Since the photo- z is used to estimate the distance to the deflectors, and from there the luminosity, total mass, and mass-to-light ratio of the mock lenses, a large error in the redshift estimation can introduce significant uncertainties on the physical properties of the mocks. Fortunately, the relative error in photo- z for almost all potential deflectors is between 10% to 30% which is low enough to be acceptable for the generation of mocks. Thus, only the catastrophic photo- z es-

timations introduce significant errors in the physical parameters of the mock lenses.

Finally, we remove bad defectors, which we define as galaxies that, based on their r -band image, would require a mass-to-light ratio larger than 12 to generate a lens with Einstein radius of $\theta_E = 1''.1$, assuming a source at redshift $z = 3.0$ and a single isothermal ellipsoid (SIE) model for the mass. We take $\theta_E = 1''.1$ because that is almost twice the average seeing, guaranteeing the visibility of the lensing features. In total, we have 649 340 galaxies useful as potential defectors. For consistency with the K-corrections and photo- z s, we use the same cosmology as SDSS for all relevant calculations, adopting flat Λ CDM with $\Omega_m = 0.2739$ and $H_0 = 70.5 \text{ km s}^{-1} \text{ Mpc}^{-1}$.

4.2. Light and mass models

To simulate the mass distribution of deflector galaxies, we use a composite model where baryons and dark matter are treated independently. This approach is preferable to power-law or isothermal models because, for this type of galaxy, the bulge and disc components dominate the lensing mass over the rounder dark halo. Furthermore, the relative proportion between the bulge, disc, and dark halo has observable effects on the lensing features.

For the baryonic part of the composite model, we use the light profile as seen in the actual data, normalised by a constant stellar mass-to-light ratio, Υ . For the dark halo component, we use a spherical Navarro-Frenk-White profile (NFW, see Navarro et al. 1996). Since the light profiles of the defectors are highly elliptical, we approximate an elliptical Sérsic profile as the difference between two cored elliptical isothermal profiles. This is known as a ‘chameleon’ profile, previously used in Dutton et al. (2011). In this work, we follow the parametrisation introduced by Suyu et al. (2014):

$$I(\boldsymbol{\xi}, w_i, q) = \frac{1}{\sqrt{\xi_1^2 + \xi_2^2/q^2 + 4w_i^2/(1+q)^2}}, \quad (6)$$

$$L_c(\boldsymbol{\xi}, w_c, w_t, q, L_0) = \frac{L_0}{1+q} [I(\boldsymbol{\xi}, w_c, q) - I(\boldsymbol{\xi}, w_t, q)], \quad (7)$$

where $\boldsymbol{\xi} \equiv (\xi_1, \xi_2) = \boldsymbol{\theta} - \boldsymbol{\theta}_0$ is the angular position relative to the centroid of the profile, q is the axis-ratio, and L_0 is the surface brightness at $1''$ from the centroid along the major axis. In addition, w_c and w_t are the sizes of the two cored isothermal profiles that are subtracted from each other, with the additional condition that $w_t > w_c$.

Because in practice our deflector galaxies can display a prominent bulge component, we also use a ‘double chameleon’ profile to model their light distribution. The double chameleon is parametrised as the sum of two concentric chameleon profiles, each one with its own ellipticity and core sizes:

$$L_d(\boldsymbol{\xi}, \mathbf{X}_1, \mathbf{X}_2, r, L_0) = L_c\left(\boldsymbol{\xi}, \mathbf{X}_1, \frac{L_0}{1+r}\right) + L_c\left(\boldsymbol{\xi}, \mathbf{X}_2, \frac{L_0}{1+1/r}\right), \quad (8)$$

where the vector $\mathbf{X}_i \equiv (w_{ic}, w_{it}, q_i)$ corresponds to the parameters for the single chameleon i , and r is the ratio between the profiles along the major axis at $1''$ away from the common centroid. We use the chameleon profiles as proxies for the baryonic mass, by replacing the normalisation L_0 with α_1 , where α_1 is now the deflection angle along the major axis at $1''$ away from the centroid.

By contrast, the spherical NFW profile is parametrised in terms of its virial mass M_{200} and concentration c . We use the scaling relations described in Duffy et al. (2008) to estimate the concentration c for every M_{200} .

We fit the chameleon and double chameleon models to the light of every potential deflector using the r -band stamps, their corresponding PSF images, and a circular pixel mask with radius $4''.5$ around the centroid of the light distributions. To do so, we use a log-likelihood that combines the standard pixel-wise noise-normalised square error with penalties for ellipticities larger than $e > 0.98$ and for negative fluxes. We minimise the log-likelihood using first a particle swarm optimiser (Kennedy & Eberhart 1995) with 200 particles and 50 iterations, and then downhill simplex optimisation (Nelder & Mead 1965) with a maximum of 3000 iterations. Then, we select between the chameleon and double chameleon models using the reduced χ^2 . Unsurprisingly, defectors with prominent bulges are better modelled by the double chameleon, while for bulgeless discs the single chameleon suffices. Good models easily reach a reduced χ^2 close 1, since we have reliable estimates of the pixel-wise noise via the RMS maps provided by the CFIS reduction pipeline. Finally, we discard defectors with reduced $\chi^2 > 3$. The whole process leaves us with a total of 558 199 potential defectors with good light models.

4.3. Reparameterising the mass models

In *Lenstronomy*, the default parametrisation of mass models is dimensionless. Instead of modelling lenses in terms of their total mass or mass density, they are parametrised based on the deflection angle caused by their associated convergence map. This approach allows for the modelling of lens systems while remaining agnostic about the exact cosmology, redshifts, and masses involved. However, when a specific cosmology and redshifts are considered, the dimensionless convergences can be interpreted as surface mass densities. This is needed to use scaling relations between the mass and the light distribution of the deflector galaxy. Since we adopt the same cosmology used in SDSS, the total convergence of each potential deflector is completely determined by the redshifts of the deflector and source, z_d , and z_s , respectively; as well as by the deflection due to the (Double) Chameleon profile α_1 , the M_{200} parameter of the NFW, and the light model of the deflector, \mathbf{L} .

However, in order to avoid ‘unphysical’ or unreal-looking lenses, we impose several constraints on the mass models. More precisely, we force the stellar mass-to-light ratio to be in the range $4.0 < \Upsilon < 9.0$, the fraction of stellar to total mass to be $0.4 < f_* < 0.8$ (baryonic fraction), and the total mass to be $10^{10} < M/M_\odot < 10^{12}$. All three quantities are calculated in the area enclosed by the tangential critical lines. In order to do this efficiently we reparameterise the total convergence from $\kappa(z_d, z_s, \mathbf{L}, \alpha_1, M_{200})$ to $\kappa(z_d, z_s, \mathbf{L}, \Upsilon, f_*)$.

For every potential deflector, we create a regular grid of parameters:

- $z_s \in \{e^x \mid x \text{ uniformly sampled between } \ln(z_d) \text{ and } \ln(3.0)\}$
- $\Upsilon \in \{4, 5, 6, 7, 8, 9\}$
- $f_* \in \{0.4, 0.48, 0.56, 0.64, 0.72, 0.8\}$

For every combination of parameters in the above grid, z_s, Υ , and f_* ; we find the corresponding combination of z_s, α_1 , and M_{200} ; such that $\kappa(z_d, z_s, \mathbf{L}, \Upsilon, f_*) = \kappa(z_d, z_s, \mathbf{L}, \alpha_1, M_{200})$. Then, we compute $\log(M)$ and θ_E . For these searches we use the bisection method as is implemented in *scipy* (Virtanen et al. 2020). For each deflector, we save all the compatible values of the

seven parameters: z_s , Υ , f_* , α_1 , $\log(M_{200})$, $\log(M)$, and θ_E . Following that, we estimate the values in-between the grid sampling using the `scikit-learn` (Pedregosa et al. 2011) implementation of the ‘Random Sample Consensus’ algorithm with a linear regression as base regressor (Fischler & Bolles 1981). We use Υ , f_* , and θ_E to predict z_s , α_1 , M_{200} , and $\log(M)$. For this regression, we normalise the data set such that each parameter has a mean of 0 and a standard deviation of 1, and generate polynomial features using a polynomial of degree 3. We take two-thirds of the sampled models for training and leave the remaining one-third for testing. We keep the interpolated values only if the accuracy on the test set is larger than 98%. This has to be done independently for each deflector, since the relationship between the seven parameters depends on the redshift of the deflector and its luminosity. The output of this procedure is a well populated grid of reasonable mass models, such that for every potential deflector and every combination of physical parameters Υ , f_* , $\log(M)$, and θ_E , we have the corresponding z_s and the `Lenstronomy` parameters α_1 , and M_{200} .

4.4. Generating a mock lens from a potential deflector

There is evidence that ML classifiers benefit from a ‘flat’ Einstein radius distribution when training on simulated lenses (Cañameras et al. 2024). Consequently, we produce the same number of mocks for every target Einstein radius, thus ensuring a flat θ_E distribution between $1''.2$ and $2''.6$, with a precision of $0''.1$.

To produce a single mock lens, we start from a deflector with a good light model, a photometric redshift, and a list of viable mass models. For simplicity, we ignore the extinction due to the disc, which reduces the apparent luminosity of the deflectors. We randomly select a mass model that complies with the physical constraints and target θ_E . This becomes the ‘target mass model’. Then, we find a potential source with a redshift equal to the value needed by the target mass model, with a tolerance of 0.02. Afterwards, we instantiate the convergence using `Lenstronomy`, and check that the total mass (M), the stellar mass-to-light ratio (Υ), and the baryonic fraction (f_*) are consistent with the target mass model. If any of the parameters is off by more than 25%, or if the sum of the relative errors is larger than 50%, we try again with a different target mass model. If this check fails twice, we skip the deflector and proceed to the next one. Otherwise, we go on to calculate the caustic lines of the system.

We randomly select between the tangential and radial caustics and place the central pixel of the source inside a polygon with the same shape as the selected caustic, but with a 15% larger perimeter. We favour the selection of the tangential over the radial caustic with a probability of 75% versus 25%. Before simulating the lensing of the source by the convergence of the deflector, we interpolate the light of the source from the *HST* image and rotate it by a random angle. The lensed image is generated with a pixel size exactly 6 times smaller than that of the deflector. We convolve the high resolution lensed source image with the corresponding PSF model of the deflector. Then, we down-sample the resulting image to the CFIS pixel size of $0''.1857$ and add Poissonian noise. The final mock lens is the sum of the deflector with the simulated image of the lensed source.

At this stage all the simulated lenses are physically motivated images mocking CFIS observations of gravitational lensing. However, the lensing features can be too faint or too blended with the deflector light, up to the point that it becomes impossible for human experts to discern the lensing features. This is often the case when simulating small Einstein radius systems and

it also affects known lenses when they are seen at worse resolution. For example, the SLACS lenses (Bolton et al. 2006), which were discovered spectroscopically and thus are rather compact, are not identified as lenses by human experts when seen on DES imaging (Rojas et al. 2023). Consequently, even if there are arcs or multiple images after simulating the lensing, that by itself is not enough to guarantee that the lensing features are visible and identifiable as such in the final image. This is especially problematic when simulating lensing by edge-on late-type galaxies because their light profiles tend to be extended and to have sub-structure; thus, increasing the chances of blending between the deflector light and the lensed source. We address this problem by implementing a ‘contrast check’ to detect if the lensing features are visible in the final image. If a mock fails the contrast check, we change the position of the source relative to the caustic lines and generate a new mock lens. If the new mock also fails the contrast check, we reject it and proceed to the next potential deflector. The details of the contrast check are presented in Appendix A. Finally, we show a sample of 56 mock lenses with different Einstein radius in Fig. B.1.

5. Finding lenses with CMU DeepLens

We use the CNN CMU DeepLens (Lanusse et al. 2018) for the binary classification task. This is a residual neural network (ResNet, see He et al. 2016a,b) explicitly designed for lens finding. It is the best performing entry in ‘‘The strong gravitational lens finding challenge’’ (Metcalfe et al. 2019) and a modified version has been successfully used in multiple lens finding efforts (Huang et al. 2020, 2021; Storfer et al. 2024; Shu et al. 2022). We reimplement the network and train it from scratch using the PyTorch framework (Paszke et al. 2019).

5.1. Training

The data set consists of 150 000 cutouts of 66×66 pixels with a pixel size of $0''.1857$. The data set is balanced, with 75 000 simulated lenses following the prescriptions of Sect. 4, and an equal number of non-lenses. The simulated lenses are distributed uniformly across a range of Einstein radii between $1''.2$ and $2''.6$, with exactly 5000 mocks per $0''.1$ bin. We present in Fig. B.1 a mosaic with some of the mock lenses in this sample. For the non-lenses, we reuse the stamps inspected in Sect. 3 and keep a flat distribution in magnitude by randomly selecting 18 750 sources per magnitude bin. By doing so, we guarantee the absence of potential lens candidates in the negative training set.

We split the data set into three parts: a training set, with 80% of the sources; and validation and test sets, each with 10% of the sources. The subsets are kept balanced, with an equal number of lenses and non-lenses. During training, each image goes through the following data processing steps:

1. random rotation up to 180° using a bilinear interpolation;
2. cropping down to 55 pixels with a new central pixel randomly selected up to 11 pixels away from the previous centre, effectively shifting the image up to $2''$;
3. vertical flip with a 50% chance;
4. normalisation to mean 0 and standard deviation 1.

During inference, the images are still cropped to 55 pixels and normalised, but the central pixel remains fixed.

We train the model by optimising a cross-entropy loss function using a stochastic gradient descent (SGD) optimiser with an initial learning rate of 10^{-3} and a momentum of 0.9. The weights

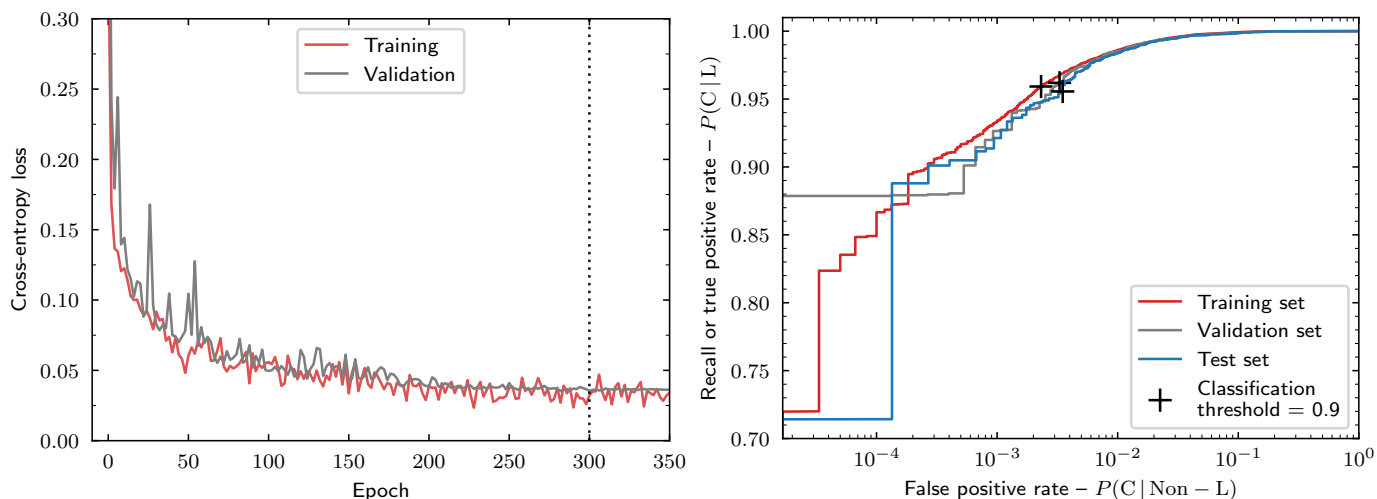


Fig. 4. Validation metrics for our training of CMU DeepLens. All the data sets are balanced. *Left*: minimisation of the loss function during training. The dotted line marks the epoch with the best validation loss. *Right*: Receiver operating characteristic (ROC) curves for the selected model. The area under the curve is 0.9993, 0.9992, and 0.9992 for the training, validation and test data sets, respectively. The “+” marks the values at the classification threshold 0.9.

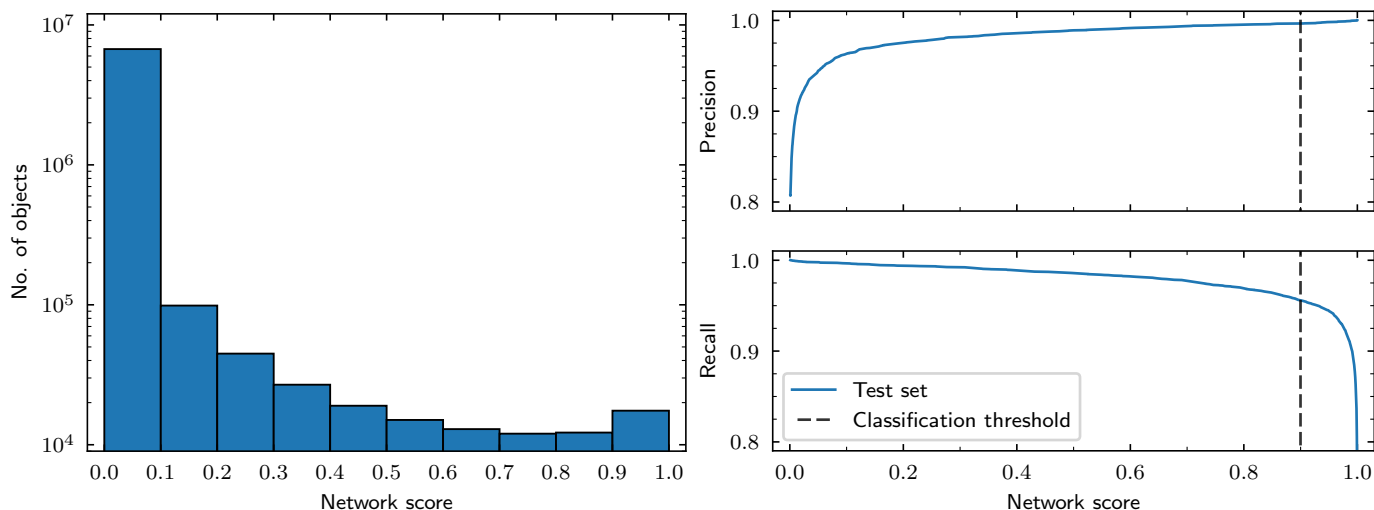


Fig. 5. *Left*: histogram in logarithmic scale of the distribution of network scores for the full parent sample, only 17 514 of the sources had a score larger than 0.9. *Right*: precision and recall versus network score for the test data set. The dashed line marks the classification threshold applied on the parent sample, 0.9. We balance the precision, recall, and number of sources selected to settle on a classification threshold.

of the network are updated using the loss calculated on the training data, while monitoring the loss on the validation set at the end of every training epoch. If the loss on the validation set does not improve for 20 consecutive epochs, then the learning rate is reduced to half its current value, down to a minimum learning rate of 10^{-8} , at which the learning rate is kept constant. The training ends after 50 consecutive epochs without improvement of the validation loss, training for a total for 350 epochs, with the best validation loss being at the 300th epoch. The batch size during training is 512 and the images are shuffled at every epoch. Overall, the training takes 17 hours on an NVIDIA GeForce GTX 1080 Ti graphics card.

5.2. Metrics and inference

We monitor the evolution of the loss function on both the training and validation data sets. This is shown in the left panel of Fig. 4. The trends of these two sets exhibit no significant divergence, suggesting that overfitting on the training set is not

a concern. In the right panel of Fig. 4, we present the ROC curve for the training, validation, and test sets. The performance of the algorithm is remarkably consistent across the three data sets, with a marginally better performance on the training set, although, this difference is negligible. Furthermore, the performance of the trained network on the test and validation data sets is, at first glance, very good, with an area under the ROC curve of 0.9992, very close to the optimal 1.0. However, this performance is underestimating the false positive rate when applied to the parent sample. Because of the extremely low prevalence of edge-on lenses, estimated to be 1 in 30 000 in Sect. 3, the classifier must have a false positive rate of the order of 1/30 000 for the sample of CNN-selected lens candidates to have a purity of 50%. Failing this, the network will suggest hundreds of false positives per actual edge-on lens candidate.

We apply the trained network to the full parent sample, yielding a network score for each of the 6 978 977 sources. The distribution of these scores is presented in the left panel of Fig. 5. We use the distribution of scores, together with the precision and

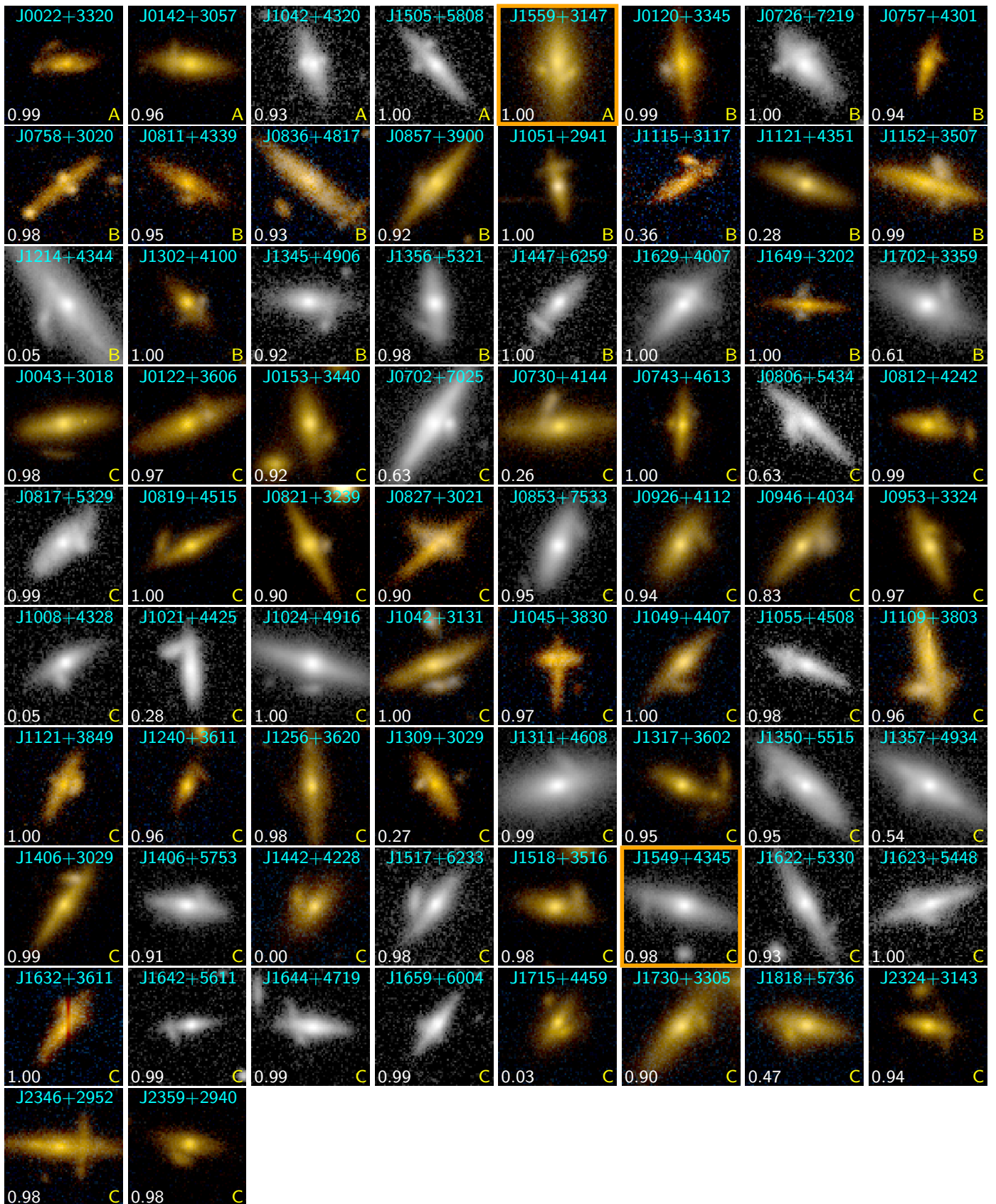


Fig. 6. Edge-on lens candidates identified by the trained CNN, or discovered serendipitously either by prototypes of the classifier or while preparing the mock lenses. They correspond to five grade A, 20 grade B, and 59 grade C; of which only two are already known. The layout follows the same scheme from Fig. 2.

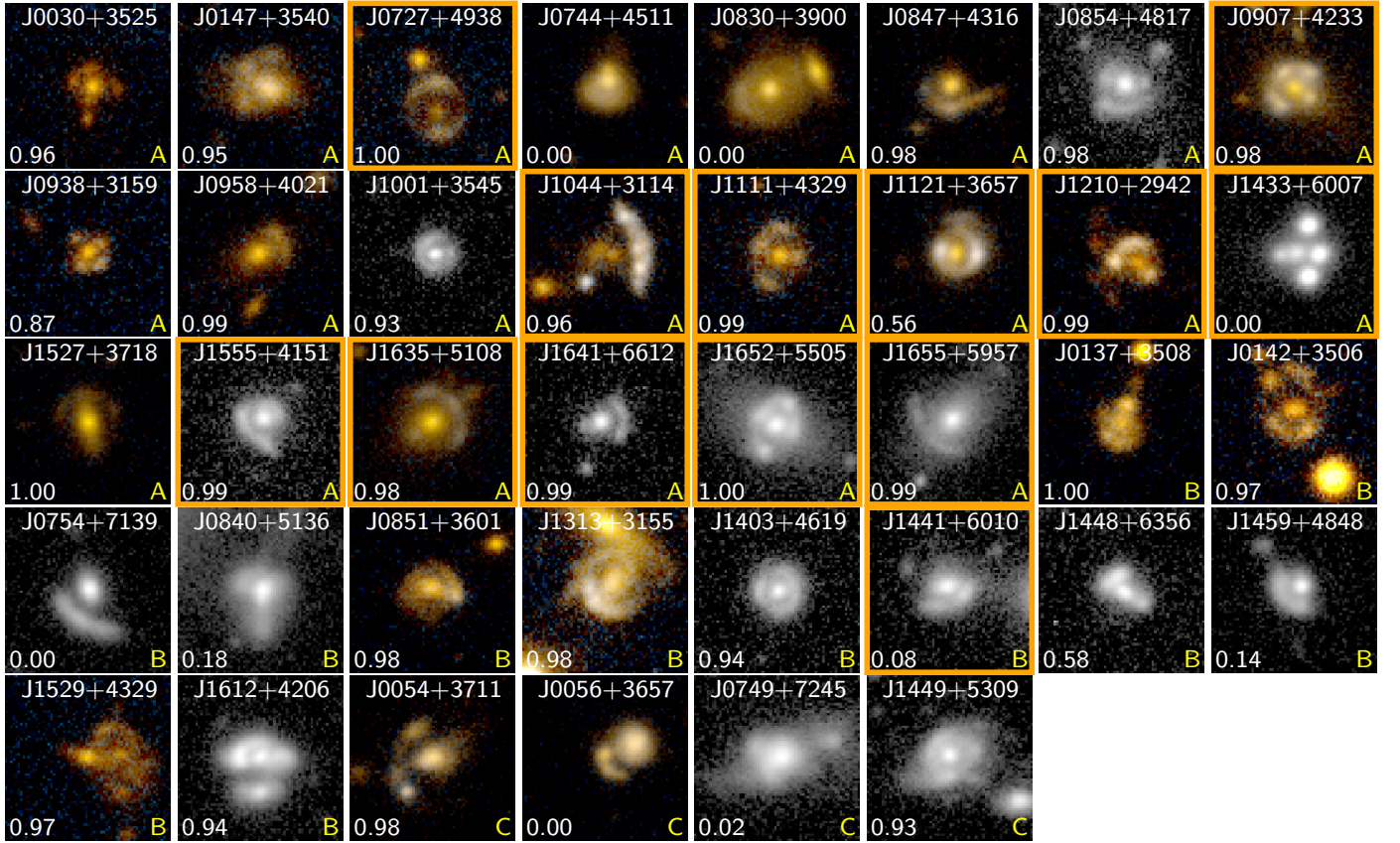


Fig. 7. Non-edge-on lens candidates identified by the trained CNN, or discovered serendipitously either by prototypes of the classifier or while preparing the mock lenses. The layout follows the same scheme from Fig. 2. The 38 candidates correspond to 22 grade A, 12 grade B, and four grade C. Of which, 12 are reported in SLED.

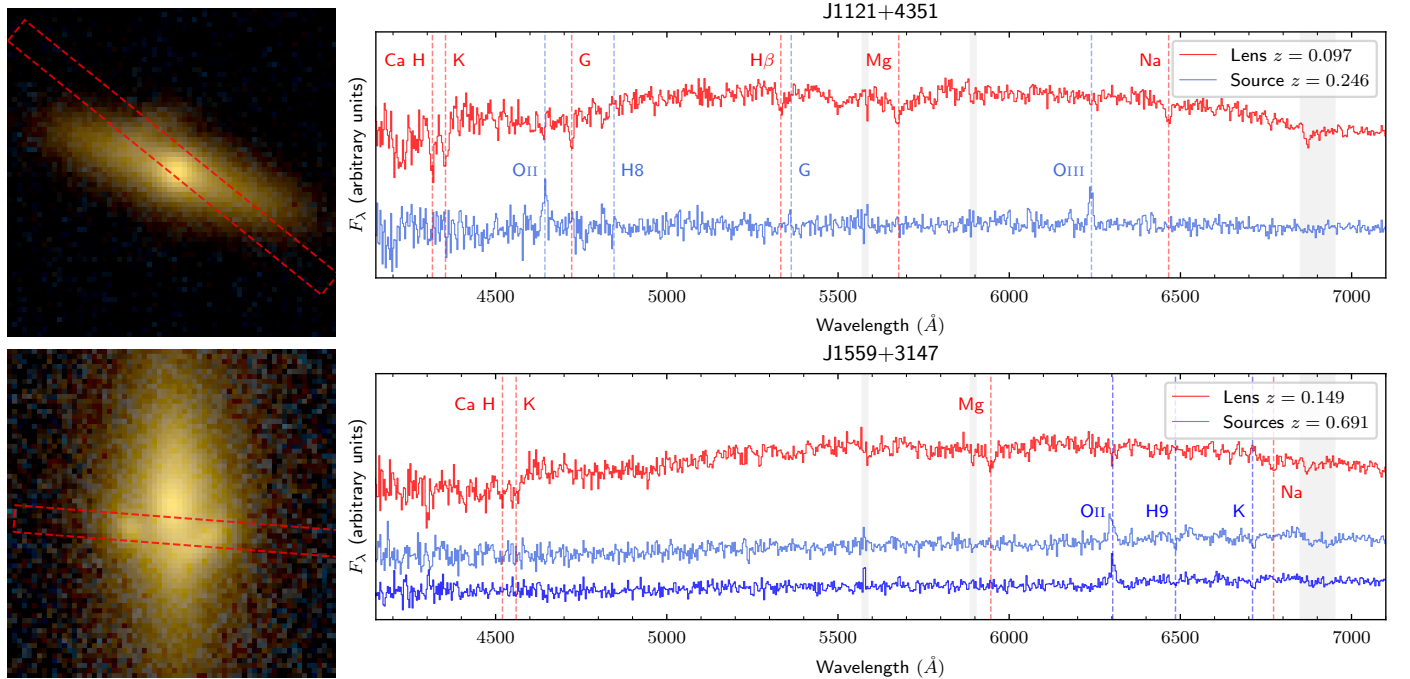


Fig. 8. Follow-up observations for J1121+4351 and J1559+3147. *Left:* UNIONS *r*-band and *u*-band imaging of the lens candidates. The red dashed line represents the slit position. *Right:* reduced 1D spectra from long-slit spectroscopy taken with the Alhambra Faint Object Spectrograph and Camera (ALFOSC) instrument in the NOT. The grey-shaded area marks atmospheric absorption bands.

recall curves evaluated on the test set, to choose a reasonable classification threshold for the parent sample. This is shown in

the right panel of Fig. 5. We select a classification threshold of 0.9, which balances a tolerable number of false positives with the

potential number of lenses to be discovered. In total, the network suggests 17 514 potential candidates.

Lastly, given the ROC curve in the right panel of Fig. 4, this threshold represents a recall of 95% and a false positive rate of 3×10^{-3} in the test set. By factoring in the edge-on lens prevalence, $P(L) \approx 1/30\,000$, we can use Eq. (3) to estimate the purity of the network-selected sample: $P(L|C) \approx 1\%$, or 180 edge-on lens candidates in the 17 514 sources selected by the network. Since we include the prevalence of edge-on lenses in our calculation, any significant deviation from this estimate shows the effects of using mock images in the test set.

5.3. Visual inspection of CNN candidates

Before visually inspecting the sample selected by the CNN, we removed the candidates discovered during the characterisation of the parent sample, that is, the sources presented in Fig. 2. We then applied the same three-step visual inspection methodology introduced in Sect. 3. The first two steps of the visual inspection were performed by J.A.A.B., B.C., and F.C., while the final group inspection was conducted by J.A.A.B., B.C., F.C., C.L., R.G., and K.R. After the first two steps, 107 sources were selected for the group inspection. To that sample, we added lens candidates discovered while prototyping our implementation of CMU DeepLens, as well as serendipitous candidates discovered while preparing the simulations used to train the network. In total, 144 sources were inspected by the six experts in the final 1-by-1 group inspection.

The final inspection yielded a total of 112 lens candidates, consisting of 27 grade A, 31 grade B, and 54 grade C objects. Focusing on edge-on lenses, we found 74 candidates: 5 grade A, 19 grade B, and 50 grade C. Notably, the majority of edge-on lens candidates are grade C, mainly due to the blending of deflector light with lensed images, and the lower lensing cross-section of late-type galaxies compared to LRGs. All the edge-on lens candidates are presented in Fig. 6, whilst the non-edge-on candidates are displayed in Fig. 7.

6. NOT spectroscopy

We obtained long-slit spectroscopic follow-up for two lens candidates using the ALFOSC instrument at the Nordic Optical Telescope (NOT) over two consecutive nights: 14 and 15 of April, 2023. For each lens candidate, we acquired two 1200 s observations using grism 4 with a $1''$ -wide slit, providing a spectral resolution of $3.3 \text{ \AA pixel}^{-1}$ and a wavelength coverage spanning 3200 \AA to 9600 \AA . The average seeing during the observations was $0''.9$.

The selected lens candidates are: J1559+3147, a grade A edge-on lens candidate previously reported in Cañameras et al. (2020) and Savary et al. (2022); and J1121+4351, a newly discovered grade B edge-on candidate. Both candidates have existing SDSS spectra, which provide the redshift of the deflectors. However, although the potential lensing features of J1121+4351 are within the SDSS fibre, the SDSS model residuals lack sufficient signal-to-noise to constrain the redshift of the source. By contrast, the brightest lensing features of J1559+3147 are outside the SDSS fibre aperture. Overall, they are well-suited candidates for confirmation with single-epoch long-slit spectroscopy focused on the lensing features.

We reduced the observations and extracted calibrated 1D spectra following the methodology of Lemon et al. (2023) and Dux et al. (2024). In brief, the 2D spectra were bias-subtracted

and cosmic rays masked using a threshold in the absolute Laplacian. A spatially-resolved background was then estimated and removed using the median value around the trace, and an error map was generated by combining background and Poissonian noise. A wavelength solution was obtained by fitting HeNe arc exposures, and refined by fitting against sky lines. The 1D spectra were extracted by dividing the trace into discrete wavelength bins and fitting a Moffat profile to each source in the trace (3 for J1559+3147 and 2 for J1121+4351) at every wavelength bin. The parameters of the Moffat profile were then interpolated using a polynomial fit, enabling accurate recovery of the 1D spectra even if the trace shifts spatially. Finally, the 1D spectra were derived by evaluating the Moffat profiles at every wavelength. Following this step, we applied flux calibration using the spectrum of the standard star Feige 34. The resulting 1D spectra are presented in Fig. 8.

Regarding the measurement of redshifts, we find for the deflector galaxy in J1121+4351 a series of absorption lines: Ca H and K, Fe G, Mg, and Na, which allows us to confirm the SDSS measurement of $z_d = 0.097$. For the potential background source, we detect the emission lines [O II] and [O III], indicating star formation and a redshift of $z_s = 0.246$. This higher redshift is consistent with the lensing hypothesis, suggesting that the source is a lensed arc. However, the lack of detection of a counter image, combined with the ground-based resolution of CFHT, prevents us from making a definitive confirmation. Higher resolution imaging is required. Promisingly, the Euclid Wide Survey will provide high-resolution observations for most of the lens candidates discovered in this work. This is crucial for edge-on lenses since they have a fair chance of being in a naked-cusp configuration, leading to the absence of a radial counter image, and thus requiring high-resolution imaging to better identify tangential lensed features. In the case of J1559+3147, we observe that the blue spectra share identical features, confirming that they are in fact two images of a single source. Furthermore, we identify [O II] in emission and K in absorption, which we use to obtain a redshift measurement: $z_s = 0.691$. Also, we identify Ca H and K, Mg, and Na in absorption in the spectrum of the deflector, confirming the SDSS redshift: $z_d = 0.149$. Remarkably, neither deflector shows emission lines.

7. Discussion

We cross-match the coordinates of all the lens candidates against the Strong Lens Database (SLED, Vernardos et al., in prep.), and summarise the results in Table 2. Overall, out of the 149 candidates identified in this work (grade A, B, and C), only 17 have been reported in SLED, including two out of the 82 edge-on lens candidates. This is consistent with the idea that edge-on lenses are missed in lens searches unless they are explicitly targeted. On the other hand, given the lack of high-resolution imaging and spectroscopic data, our search is susceptible to contamination by recent mergers and random alignments of galaxies. But, the UNIONS footprint overlaps with that of *Euclid*, guaranteeing high-resolution imaging for all of the candidates in the next five years. This will allow us to confirm or refute many of the candidates, especially in the grade C category.

Regarding our lens finding methodology, specifically the use of a CNN trained and validated on simulations, we note that the validation metrics presented in Sect. 5.2 overestimate the performance of the classifier when applied to the parent sample. In Sect. 5.2, we used the prevalence of edge-on lensing as estimated in Sect. 3, along with the recall and false positive rate of the CNN estimated on the test set, to predict 180 edge-on lenses

Table 2. Summary results of the lens search. This includes all candidates regardless of how they were found. We cross-match our whole sample of lens candidates against the the Strong Lens Database (SLED) to identify the new candidates. We marginalise by grade, and present results for both strong lensing in general, and edge-on lenses only.

Grade	Any deflector		Edge-on deflector	
	Total candidates	New candidates	Total candidates	New candidates
A	35	20	5	4
B	37	36	20	20
C	77	76	59	58
All grades	149	132	84	82

Table 3. Summary of the performance of the CNN in identifying *edge-on lenses*. The metrics are marginalised by grade and magnitude bin to enable direct comparison with Table 1. We present the number of candidates found, the expected number of candidates based on Table 1, and the completeness (number found / expected number). We also include the fraction of lens candidates among sources inspected for the CNN-selected sample and for the randomly selected sample, respectively; and the ratio between these two, corresponding to the boost in lensing prevalence due to the CNN selection relative to the random selection.

Grade	Mag. bin	Candidates found	Candidates expected	Completeness	Purity of the CNN sample	Prevalence in parent sample	Ratio of CNN-purity to base prevalence
A+B	17 to 18	4	11	36%	7.7×10^{-3}	3.3×10^{-5}	231.2
A+B	18 to 19	7	< 37	> 19%	1.9×10^{-3}	0	
A+B	19 to 20	10	< 108	> 9%	1.1×10^{-3}	0	
A+B	20 to 20.5	0	< 106	0	0	0	
C	17 to 18	9	55	16%	1.7×10^{-2}	1.7×10^{-4}	104.0
C	18 to 19	21	100	21%	5.6×10^{-3}	1.0×10^{-4}	56.2
C	19 to 20	11	95	12%	1.2×10^{-3}	3.3×10^{-5}	35.7
C	20 to 20.5	1	< 106	> 1%	2.5×10^{-4}	0	

Table 4. Summary of the performance of the CNN in identifying lens candidates with any type of deflector. This table follows the layout of Table 3.

Grade	Mag. bin	Candidates found	Candidates expected	Completeness	Purity of the CNN sample	Prevalence in parent sample	Ratio of CNN-purity to base prevalence
A+B	17 to 18	4	55	7%	7.7×10^{-3}	1.7×10^{-4}	46.2
A+B	18 to 19	13	100	13%	3.5×10^{-3}	1.0×10^{-4}	34.8
A+B	19 to 20	21	380	6%	2.3×10^{-3}	1.3×10^{-4}	17.0
A+B	20 to 20.5	8	187	4%	2.0×10^{-3}	6.7×10^{-5}	29.9
C	17 to 18	9	120	8%	1.7×10^{-2}	3.7×10^{-4}	47.3
C	18 to 19	22	200	11%	5.9×10^{-3}	2.0×10^{-4}	29.4
C	19 to 20	12	190	6%	1.3×10^{-3}	6.7×10^{-5}	19.5
C	20 to 20.5	1	374	0%	2.5×10^{-4}	1.3×10^{-4}	1.9

Table 5. Completeness of the entire lens search, including the candidates discovered by the CNN, the candidates discovered serendipitously, and the candidates discovered during the initial characterisation of the sample. We use the estimates from Table 1 for the expected total number of candidates.

Grade	Mag. bin	Edge-on deflector			Any deflector		
		Candidates found	Candidates expected	Completeness	Candidates found	Candidates expected	Completeness
A+B	17 to 18	7	11	64%	12	55	22%
A+B	18 to 19	7	< 37	> 19%	18	100	18%
A+B	19 to 20	10	< 108	> 9%	30	380	8%
A+B	20 to 20.5	1	< 106	> 1%	12	187	6%
C	17 to 18	17	55	31%	24	120	20%
C	18 to 19	26	100	26%	30	200	15%
C	19 to 20	15	95	16%	17	190	9%
C	20 to 20.5	1	< 106	> 1%	6	374	2%

in the 17 514 sources selected by the network. However, only 63 (35% of the predicted number) edge-on lenses were found during the visual inspection among the CNN-selected candidates. This implies that the use of a simulated test set leads to overestimating the purity of the network by at least a factor of two. We believe this to be a consequence of imperfect domain adaptation, and that it mainly affects $P(C|L)$, the classifier’s ability to identify a real lens as a lens. Since the classifier is trained on simulations, it is expected that its performance worsens when applied to real lenses. However, this should be kept in mind when evaluating different networks and classification schemes, which is routinely done using metrics calculated on data sets dominated by mock lenses.

As an alternative to the use of metrics calculated on simulated data sets, we evaluate the effectiveness of our lens search methodology by comparing the CNN-selected sample against the sample that we use in Sect. 3 to characterise the parent sample. In short, we expect the CNN-selected sample to have a higher prevalence of edge-on lenses than the parent sample, while retaining as many edge-on lenses as possible. We present these metrics in Table 3 for edge-on lenses, and in Table 4 for lensing in general. We note that using the network increases the prevalence of grade A and B edge-on lensing by up to two orders of magnitude, going from 1/30 000 to 1/130 in the brightest magnitude bin, but at the cost of recovering only 36% of the lenses. However, the situation is less straightforward for the fainter edge-on lenses, since their prevalence is so low that we did not find a single instance of them when characterising the parent sample. In those cases, our estimates of the completeness are calculated against the upper bounds presented in Table 1. Nonetheless, we did find 17 edge-on lens candidates grade A and B with magnitudes between 18 and 20 in the CNN-selected sample, indicating that the CNN is sensitive to them. We also observe in the last column of Tables 3 and 4, that the improvement in the prevalence decreases with magnitude, which can be explained by the reduced contrast between the lensing features and the deflector’s light, leading to noisier classifications by the CNN. Similarly, the ratio is lower for grade C candidates, being around 100 compared with 230 for the grade A and B. This suggests that the CNN performs best against clear lens candidates, such as those with higher visual inspection grades and brighter features.

Regarding the objects missed by the CNN, they amount to 4 grade B and 17 grade C edge-on lens candidates. Notoriously, all of the grade A edge-on lens candidates presented in this work are also part of the CNN-selected sample. Similarly, there are 12 grade A, 10 grade B, and 16 grade C non-edge-on lens candidates that the CNN missed. Given a total of 65 non-edge-on lens candidates, the 38 candidates missed by the CNN represent the majority of the sample. This is expected since the training of the network does not include examples of other types of lenses.

Lastly, we present in Table 5 the completeness of the whole search, including all the candidates regardless of how they were identified. The search is about 64% complete for the grade A and B edge-on lens candidates in brightest magnitude bin (17 to 18), and at least 19% and 9% complete for those brighter than 19 and 20 magnitudes, respectively. Regarding the grade C, our search finds 31% of the brightest edge-on lens candidates, and around 20% of those with magnitudes between 18 and 20. However, even after including the serendipitous discoveries, our search still fails to find a significant number of edge-on lens candidates in the faintest magnitude bin. Hinting that at magnitudes fainter than 20, the signal-to-noise ratio (SNR) falls below the

minimum threshold at which we can identify the lensing features.

8. Conclusions

We performed a lens search targeting edge-on late-type galaxies in 3600 deg² of UNIONS *r*-band data using a CNN. We discovered 4 grade A, 20 grade B, and 58 grade C edge-on lens candidates; as well as 16 grade A, 16 grade B, and 18 grade C lens candidates that are not edge-on. This represents a significant increase in the sample of known edge-on lens candidates, previously on the order of a hundred. Furthermore, we estimate that our new candidates encompass between 9% and 60% of all the discoverable edge-on lens candidates in the parent sample, as determined by the initial inspection of the data in Sect. 3.

We characterised the parent sample by performing a visual inspection of 120 000 randomly selected sources. This allowed us to establish a baseline against which we can measure the performance of the CNN in the lens finding task. Moreover, using Bayes’ theorem, we extrapolated the number of candidates found among the randomly selected sources, to estimate the total number of lens candidates in the parent sample. Overall, we estimate that there are at least 8 grade A and B, and about 250 grade C edge-on lens candidates in the entire parent sample. This is consistent with a prevalence rate of one edge-on lens candidate for every 30 000 sources. Also, for lensing in general, we find the prevalence rate to be consistent with one lens candidate for every 10 000 sources.

Regarding the performance of the CNN classifier, we showed that metrics calculated on simulated data sets significantly overestimate the performance of the network. Thus, we advise against using metrics calculated on simulations. As an alternative, we have used our initial characterisation of the sample to directly evaluate the performance of automatic classifiers without relying on simulated data sets. That is, by comparing the number of lenses and purity of the CNN-selected sample to the estimated number of lenses and prevalence of lensing in the parent sample. An ideal classifier would select all of the lenses estimated to be in the parent sample, and nothing else, resulting in a purity of 1 and a false-positive rate of 0. We propose that future lens searches follow a similar methodology when evaluating their classifiers. Reporting both the completeness of their sample and the ratio between the purity of the sample and the estimated prevalence of lensing in the parent sample.

To create a training set for the CNN, we developed a data-driven methodology that allows us to systematically generate mock observations of edge-on lenses. Our mock observations use real *r*-band UNIONS observations for the deflector light, and deep *HST* observations for the source light, which improves the realism of the simulated images. Moreover, the simulated lenses had a realistic mass model, with a stellar-mass-to-light ratio, baryonic fraction, and total mass within the accepted ranges for edge-on lenses, ensuring the simulated lenses are physically plausible.

We spectroscopically followed-up two of our edge-on lens candidates: J1121+4351 and J1559+3147. For the former, we confirmed the redshift of the deflector to be $z_d = 0.097$ and measured the redshift of the arc at $z_s = 0.246$, but given the lack of clear counter image, high-resolution imaging is still required to confirm its lensing nature. By contrast, the spectra of the lensed images of J1559+3147 showed identical features, confirming its lensing nature; we measured the redshift of the deflector at $z_d = 0.149$ and the lensed source at $z_s = 0.691$.

Finally, we proved the feasibility of finding edge-on lenses in large-area optical surveys using artificial intelligence, as long as the lens search targets edge-on lenses explicitly. However, even though the UNIONS r -band data have an excellent average seeing ($0''.6$), we have hit the limitations of ground-based observations. The lower lensing cross-section of late-type galaxies, combined with their extended spatial features, results in most lens candidates suffering from blending between the light of the deflector and the lensing features. This makes it challenging for human experts to identify lens candidates during visual inspection and can also confuse CNN classifiers. This is evident in the decrease in the number of candidates found as the magnitude increases. Thus, we conclude that to identify the bulk of the late-type galaxy lenses, it is necessary to mine surveys with even higher resolution. This is already the case with HSC, which was providing most of the new edge-on late-type lens candidates before this work. However, the most significant step forward will come from *Euclid*, which will observe $14\,000\text{ deg}^2$ with an average resolution of $0''.2$, combining a large volume probed with superb resolution. Thus, making it the most promising target for future searches of lensing by edge-on late-type galaxies.

Acknowledgements. We thank Elodie Savary for fruitful discussions in the early stages of this work. J. A. A. B., B. C., F. C., and K. R. acknowledge support from the Swiss National Science Foundation (SNSF). Funded by a Royal Society University Research Fellowship. This project has received funding from the European Research Council (ERC) under the European Union's Horizon 2020 research and innovation programme (LensEra: grant agreement No 945536). We are honoured and grateful for the opportunity of observing the Universe from Maunakea and Haleakala, which both have cultural, historical and natural significance in Hawaii. This work is based on data obtained as part of the Canada-France Imaging Survey, a CFHT large program of the National Research Council of Canada and the French Centre National de la Recherche Scientifique. Based on observations obtained with MegaPrime/MegaCam, a joint project of CFHT and CEA Saclay, at the Canada-France-Hawaii Telescope (CFHT) which is operated by the National Research Council (NRC) of Canada, the Institut National des Science de l'Univers (INSU) of the Centre National de la Recherche Scientifique (CNRS) of France, and the University of Hawaii. This research used the facilities of the Canadian Astronomy Data Centre operated by the National Research Council of Canada with the support of the Canadian Space Agency. This research is based in part on data collected at Subaru Telescope, which is operated by the National Astronomical Observatory of Japan. Pan-STARRS is a project of the Institute for Astronomy of the University of Hawaii, and is supported by the NASA SSO Near Earth Observation Program under grants 80NSSC18K0971, NNX14AM74G, NNX12AR65G, NNX13AQ47G, NNX08AR22G, 80NSSC21K1572 and by the State of Hawaii. Based on observations made with the Nordic Optical Telescope, owned in collaboration by the University of Turku and Aarhus University, and operated jointly by Aarhus University, the University of Turku and the University of Oslo, representing Denmark, Finland and Norway, the University of Iceland and Stockholm University at the Observatorio del Roque de los Muchachos, La Palma, Spain, of the Instituto de Astrofísica de Canarias. Horizon 2020/2021-2025: This project has received funding from the European Union's Horizon 2020 research and innovation programme under grant agreement No 101004719 (ORP: OPTICON RadioNet Pilot). The Legacy Surveys consist of three individual and complementary projects: the Dark Energy Camera Legacy Survey (DECaLS; Proposal ID #2014B-0404; PIs: David Schlegel and Arjun Dey), the Beijing-Arizona Sky Survey (BASS; NOAO Prop. ID #2015A-0801; PIs: Zhou Xu and Xiaohui Fan), and the Mayall z -band Legacy Survey (MzLS; Prop. ID #2016A-0453; PI: Arjun Dey). DECaLS, BASS and MzLS together include data obtained, respectively, at the Blanco telescope, Cerro Tololo Inter-American Observatory, NSF's NOIRLab; the Bok telescope, Steward Observatory, University of Arizona; and the Mayall telescope, Kitt Peak National Observatory, NOIRLab. Pipeline processing and analyses of the data were supported by NOIRLab and the Lawrence Berkeley National Laboratory (LBNL). The Legacy Surveys project is honoured to be permitted to conduct astronomical research on Iolkam Du'ag (Kitt Peak), a mountain with particular significance to the Tohono O'odham Nation. NOIRLab is operated by the Association of Universities for Research in Astronomy (AURA) under a cooperative agreement with the National Science Foundation. LBNL is managed by the Regents of the University of California under contract to the U.S. Department of Energy. This project used data obtained with the Dark Energy Camera (DECam), which was constructed by the Dark Energy Survey (DES) collaboration. Funding for the DES Projects has been provided by the U.S. Department of Energy, the U.S. National Science Foundation, the Ministry

of Science and Education of Spain, the Science and Technology Facilities Council of the United Kingdom, the Higher Education Funding Council for England, the National Center for Supercomputing Applications at the University of Illinois at Urbana-Champaign, the Kavli Institute of Cosmological Physics at the University of Chicago, Center for Cosmology and Astro-Particle Physics at the Ohio State University, the Mitchell Institute for Fundamental Physics and Astronomy at Texas A&M University, Financiadora de Estudos e Projetos, Fundação Carlos Chagas Filho de Amparo, Financiadora de Estudos e Projetos, Fundação Carlos Chagas Filho de Amparo a Pesquisa do Estado do Rio de Janeiro, Conselho Nacional de Desenvolvimento Científico e Tecnológico and the Ministerio da Ciência, Tecnologia e Inovação, the Deutsche Forschungsgemeinschaft and the Collaborating Institutions in the Dark Energy Survey. The Collaborating Institutions are Argonne National Laboratory, the University of California at Santa Cruz, the University of Cambridge, Centro de Investigaciones Energéticas, Medioambientales y Tecnológicas-Madrid, the University of Chicago, University College London, the DES-Brazil Consortium, the University of Edinburgh, the Eidgenössische Technische Hochschule (ETH) Zurich, Fermi National Accelerator Laboratory, the University of Illinois at Urbana-Champaign, the Institut de Ciències de l'Espai (IEEC/CSIC), the Institut de Física d'Altes Energies, Lawrence Berkeley National Laboratory, the Ludwig Maximilians Universität München and the associated Excellence Cluster Universe, the University of Michigan, NSF's NOIRLab, the University of Nottingham, the Ohio State University, the University of Pennsylvania, the University of Portsmouth, SLAC National Accelerator Laboratory, Stanford University, the University of Sussex, and Texas A&M University. BASS is a key project of the Telescope Access Program (TAP), which has been funded by the National Astronomical Observatories of China, the Chinese Academy of Sciences (the Strategic Priority Research Program "The Emergence of Cosmological Structures" Grant No. XDB09000000), and the Special Fund for Astronomy from the Ministry of Finance. The BASS is also supported by the External Cooperation Program of Chinese Academy of Sciences (Grant No. 114A11KYSB20160057), and Chinese National Natural Science Foundation (Grant No. 12120101003, No. 11433005). The Legacy Surveys imaging of the DESI footprint is supported by the Director, Office of Science, Office of High Energy Physics of the U.S. Department of Energy under Contract No. DE-AC02-05CH1123, by the National Energy Research Scientific Computing Center, a DOE Office of Science User Facility under the same contract; and by the U.S. National Science Foundation, Division of Astronomical Sciences under Contract No. AST-0950945 to NOAO. Funding for the Sloan Digital Sky Survey IV has been provided by the Alfred P. Sloan Foundation, the U.S. Department of Energy Office of Science, and the Participating Institutions. SDSS-IV acknowledges support and resources from the Center for High Performance Computing at the University of Utah. The SDSS website is www.sdss4.org. SDSS-IV is managed by the Astrophysical Research Consortium for the Participating Institutions of the SDSS Collaboration including the Brazilian Participation Group, the Carnegie Institution for Science, Carnegie Mellon University, Center for Astrophysics | Harvard & Smithsonian, the Chilean Participation Group, the French Participation Group, Instituto de Astrofísica de Canarias, The Johns Hopkins University, Kavli Institute for the Physics and Mathematics of the Universe (IPMU) / University of Tokyo, the Korean Participation Group, Lawrence Berkeley National Laboratory, Leibniz Institut für Astrophysik Potsdam (AIP), Max-Planck-Institut für Astronomie (MPIA Heidelberg), Max-Planck-Institut für Astrophysik (MPA Garching), Max-Planck-Institut für Extraterrestrische Physik (MPE), National Astronomical Observatories of China, New Mexico State University, New York University, University of Notre Dame, Observatório Nacional / MCTI, The Ohio State University, Pennsylvania State University, Shanghai Astronomical Observatory, United Kingdom Participation Group, Universidad Nacional Autónoma de México, University of Arizona, University of Colorado Boulder, University of Oxford, University of Portsmouth, University of Utah, University of Virginia, University of Washington, University of Wisconsin, Vanderbilt University, and Yale University.

References

- Abdurro'uf, Accetta, K., Aerts, C., et al. 2022, *ApJS*, 259, 35
 Acevedo Barroso, J. A., O'Riordan, C. M., Clément, B., et al. 2024, *A&A*, submitted, arXiv:2408.06217
 Astropy Collaboration, Price-Whelan, A. M., Lim, P. L., et al. 2022, *ApJ*, 935, 167
 Atek, H., Chemerynska, I., Wang, B., et al. 2023, *MNRAS*, 524, 5486
 Auger, M. W., Treu, T., Bolton, A. S., et al. 2010, *ApJ*, 724, 511
 Barnabè, M., Dutton, A. A., Marshall, P. J., et al. 2012, *MNRAS*, 423, 1073
 Bertin, E. 2011, in *Astronomical Society of the Pacific Conference Series*, Vol. 442, *Astronomical Data Analysis Software and Systems XX*, ed. I. N. Evans, A. Accomazzi, D. J. Mink, & A. H. Rots, 435
 Birrer, S. & Amara, A. 2018, *Physics of the Dark Universe*, 22, 189
 Birrer, S., Shajib, A., Gilman, D., et al. 2021, *The Journal of Open Source Software*, 6, 3283

- Birrer, S., Shajib, A. J., Galan, A., et al. 2020, *A&A*, 643, A165
- Blanton, M. R., Bershad, M. A., Abolfathi, B., et al. 2017, *AJ*, 154, 28
- Bolton, A. S., Burles, S., Koopmans, L. V. E., Treu, T., & Moustakas, L. A. 2006, *ApJ*, 638, 703
- Bradley, L. D., Coe, D., Brammer, G., et al. 2023, *ApJ*, 955, 13
- Brewer, B. J., Dutton, A. A., Treu, T., et al. 2012, *MNRAS*, 422, 3574
- Brewer, B. J., Marshall, P. J., Auger, M. W., et al. 2014, *MNRAS*, 437, 1950
- Cañameras, R., Schuldt, S., Shu, Y., et al. 2024, *A&A*, 692, A72
- Cañameras, R., Schuldt, S., Shu, Y., et al. 2021, *A&A*, 653, L6
- Cañameras, R., Schuldt, S., Suyu, S. H., et al. 2020, *A&A*, 644, A163
- Chambers, K. C., Magnier, E. A., Metcalfe, N., et al. 2016, arXiv:1612.05560
- Chan, J. H. H., Suyu, S. H., Sonnenfeld, A., et al. 2020, *A&A*, 636, A87
- Chen, W., Kelly, P. L., Frye, B. L., et al. 2024, *ApJ*, 970, 102
- Collett, T. E. 2015, *ApJ*, 811, 20
- Czoske, O., Barnabè, M., Koopmans, L. V. E., Treu, T., & Bolton, A. S. 2012, *MNRAS*, 419, 656
- Dey, A., Schlegel, D. J., Lang, D., et al. 2019, *AJ*, 157, 168
- Duffy, A. R., Schaye, J., Kay, S. T., & Dalla Vecchia, C. 2008, *MNRAS*, 390, L64
- Dutton, A. A., Brewer, B. J., Marshall, P. J., et al. 2011, *MNRAS*, 417, 1621
- Dutton, A. A. & Treu, T. 2014, *MNRAS*, 438, 3594
- Dutton, A. A., Treu, T., Brewer, B. J., et al. 2013, *MNRAS*, 428, 3183
- Dux, F., Lemon, C., Courbin, F., et al. 2024, *A&A*, 682, A47
- Etherington, A., Nightingale, J. W., Massey, R., et al. 2022, *MNRAS*, 517, 3275
- Euclid Collaboration: Mellier, Y., Abdurro'uf, Acevedo Barroso, J., et al. 2024, *A&A*, accepted, arXiv:2405.13491
- Euclid Collaboration: Scaramella, R., Amiaux, J., Mellier, Y., et al. 2022, *A&A*, 662, A112
- Ferrami, G. & Wyithe, J. S. B. 2024, *MNRAS*, 532, 1832
- Ferreras, I., Saha, P., Leier, D., Courbin, F., & Falco, E. E. 2010, *MNRAS*, 409, L30
- Fischler, M. A. & Bolles, R. C. 1981, *Commun. ACM*, 24, 381–395
- Flewelling, H. A., Magnier, E. A., Chambers, K. C., et al. 2020, *ApJS*, 251, 7
- Gilman, D., Birrer, S., Nierenberg, A., & Oh, M. S. H. 2024, *MNRAS*, 533, 1687
- González, J., Holloway, P., Collett, T., et al. 2025, arXiv:2501.15679
- Grespan, M., Thuruthipilly, H., Pollo, A., et al. 2024, *A&A*, 688, A34
- Guinot, A., Kilbinger, M., Farrens, S., et al. 2022, *A&A*, 666, A162
- Gwyn, S. 2019, in *Astronomical Society of the Pacific Conference Series*, Vol. 523, *Astronomical Data Analysis Software and Systems XXVII*, ed. P. J. Teuben, M. W. Pound, B. A. Thomas, & E. M. Warner, 649
- Gwyn, S. D. J. 2008, *PASP*, 120, 212
- He, K., Zhang, X., Ren, S., & Sun, J. 2016a, in 2016 IEEE Conference on Computer Vision and Pattern Recognition (CVPR), 1
- He, K., Zhang, X., Ren, S., & Sun, J. 2016b, arXiv:1603.05027
- He, Z., Er, X., Long, Q., et al. 2020, *MNRAS*, 497, 556
- He, Z., Li, N., Cao, X., et al. 2023, *A&A*, 672, A123
- Huang, X., Storfer, C., Gu, A., et al. 2021, *ApJ*, 909, 27
- Huang, X., Storfer, C., Ravi, V., et al. 2020, *ApJ*, 894, 78
- Ibata, R. A., McConnachie, A., Cuillandre, J.-C., et al. 2017, *ApJ*, 848, 128
- Jacobs, C., Collett, T., Glazebrook, K., et al. 2019a, *ApJS*, 243, 17
- Jacobs, C., Collett, T., Glazebrook, K., et al. 2019b, *MNRAS*, 484, 5330
- Jaelani, A. T., More, A., Wong, K. C., et al. 2024, *MNRAS*, 535, 1625
- Kelly, P. L., Rodney, S., Treu, T., et al. 2023, *Science*, 380, abh1322
- Kennedy, J. & Eberhart, R. 1995, in *Proceedings of ICNN'95 - International Conference on Neural Networks*, Vol. 4, 1942–1948 vol.4
- Khadka, N., Birrer, S., Leauthaud, A., & Nix, H. 2024, *MNRAS*, 533, 795
- Lanusse, F., Ma, Q., Li, N., et al. 2018, *MNRAS*, 473, 3895
- Lemon, C., Anguita, T., Auger-Williams, M. W., et al. 2023, *MNRAS*, 520, 3305
- Li, R., Napolitano, N. R., Spiniello, C., et al. 2021, *ApJ*, 923, 16
- Li, R., Napolitano, N. R., Tortora, C., et al. 2020, *ApJ*, 899, 30
- Mahler, G., Jauzac, M., Richard, J., et al. 2023, *ApJ*, 945, 49
- Metcalfe, R. B., Meneghetti, M., Avstruz, C., et al. 2019, *A&A*, 625, A119
- Nagam, B. C., Acevedo Barroso, J. A., Wilde, J., et al. 2025, *A&A*, submitted, arXiv:2502.09802
- Navarro, J. F., Frenk, C. S., & White, S. D. M. 1996, *ApJ*, 462, 563
- Nelder, J. A. & Mead, R. 1965, *The Computer Journal*, 7, 308
- Nierenberg, A. M., Keeley, R. E., Sluse, D., et al. 2024, *MNRAS*, 530, 2960
- Nightingale, J. W., He, Q., Cao, X., et al. 2024, *MNRAS*, 527, 10480
- Nightingale, J. W., Smith, R. J., He, Q., et al. 2023, *MNRAS*, 521, 3298
- O'Donnell, J. H., Wilkinson, R. D., Diehl, H. T., et al. 2022, *ApJS*, 259, 27
- Oguri, M. & Marshall, P. J. 2010, *MNRAS*, 405, 2579
- Paszke, A., Gross, S., Massa, F., et al. 2019, arXiv:1912.01703
- Pedregosa, F., Varoquaux, G., Gramfort, A., et al. 2011, *Journal of Machine Learning Research*, 12, 2825
- Petrillo, C. E., Tortora, C., Chatterjee, S., et al. 2017, *MNRAS*, 472, 1129
- Petrillo, C. E., Tortora, C., Vernardos, G., et al. 2019, *MNRAS*, 484, 3879
- Rojas, K., Collett, T. E., Ballard, D., et al. 2023, *MNRAS*, 523, 4413
- Rojas, K., Savary, E., Clément, B., et al. 2022, *A&A*, 668, A73
- Savary, E., Rojas, K., Maus, M., et al. 2022, *A&A*, 666, A1
- Schuldt, S., Cañameras, R., Andika, I. T., et al. 2025, *A&A*, 693, A291
- Schuldt, S., Chirivì, G., Suyu, S. H., et al. 2019, *A&A*, 631, A40
- Shajib, A. J., Birrer, S., Treu, T., et al. 2019, *MNRAS*, 483, 5649
- Shajib, A. J., Mozumdar, P., Chen, G. C. F., et al. 2023, *A&A*, 673, A9
- Sheu, W., Shajib, A. J., Treu, T., et al. 2024, arXiv:2408.10316
- Shu, Y., Cañameras, R., Schuldt, S., et al. 2022, *A&A*, 662, A4
- Sonnenfeld, A., Jaelani, A. T., Chan, J., et al. 2019, *A&A*, 630, A71
- Stein, G., Blaum, J., Harrington, P., Medan, T., & Lukić, Z. 2022, *ApJ*, 932, 107
- Storfer, C., Huang, X., Gu, A., et al. 2024, *ApJS*, 274, 16
- Suyu, S. H., Hensel, S. W., McKean, J. P., et al. 2012, *ApJ*, 750, 10
- Suyu, S. H., Treu, T., Hilbert, S., et al. 2014, *ApJ*, 788, L35
- Syngnet, J. F., Tu, H., Fort, B., & Gavazzi, R. 2010, *A&A*, 517, A25
- Talbot, M. S., Brownstein, J. R., Dawson, K. S., Kneib, J.-P., & Bautista, J. 2021, *MNRAS*, 502, 4617
- Treu, T., Dutton, A. A., Auger, M. W., et al. 2011, *MNRAS*, 417, 1601
- Vegetti, S., Koopmans, L. V. E., Bolton, A., Treu, T., & Gavazzi, R. 2010, *MNRAS*, 408, 1969
- Virtanen, P., Gommers, R., Oliphant, T. E., et al. 2020, *Nature Methods*, 17, 261
- Wong, K. C., Suyu, S. H., Chen, G. C. F., et al. 2020, *MNRAS*, 498, 1420

Appendix A: The contrast check

In this appendix, we elaborate on the methodology of the contrast check. We use this check to determine whether the lensing features are visible above the noise background and the deflector galaxy. Since the images of both the lensed source and the deflector galaxy are sampled on the same pixel grid, we can directly compare corresponding pixels between the two images. Thus, the contrast check consists of identifying and counting the pixels that are ‘dominated by the lensed source light’. If there are enough such pixels, then the lensing features are deemed as visible and the mock passes the check. We present the details of the process with the help of Fig. A.1.

- Step 1: Estimate the background level μ and background dispersion σ of the deflector image. We calculate μ using the median, and σ using the normalised median absolute deviation (MAD).
- Step 2: Create masks for both images by selecting pixels above $\mu + 3\sigma$. Panels (a) and (b) show the deflector galaxy and lensed source images, respectively, while panels (c) and (d) display their corresponding masks.
- Step 3: Identify and count the pixels in the lensed source mask that do not overlap with the deflector mask. These pixels, shown in white in panel (e), are considered dominated by the lensed source. If fewer than five such pixels are found, the contrast check fails.
- Step 4: Identify overlapping pixels between the two masks, which are displayed in grey in panel (e).
- Step 5: Count the overlapping pixels that are dominated by the lensed source light.
- Step 6: The total number of pixels dominated by the lensed source light must be larger than 20, and they must amount to at least 30% of the pixels in the lensed source mask. Panel (f) presents all the pixels dominated by the lensed source light.

Finally, we show the final mock lens, which passes the contrast check, in panel (g).

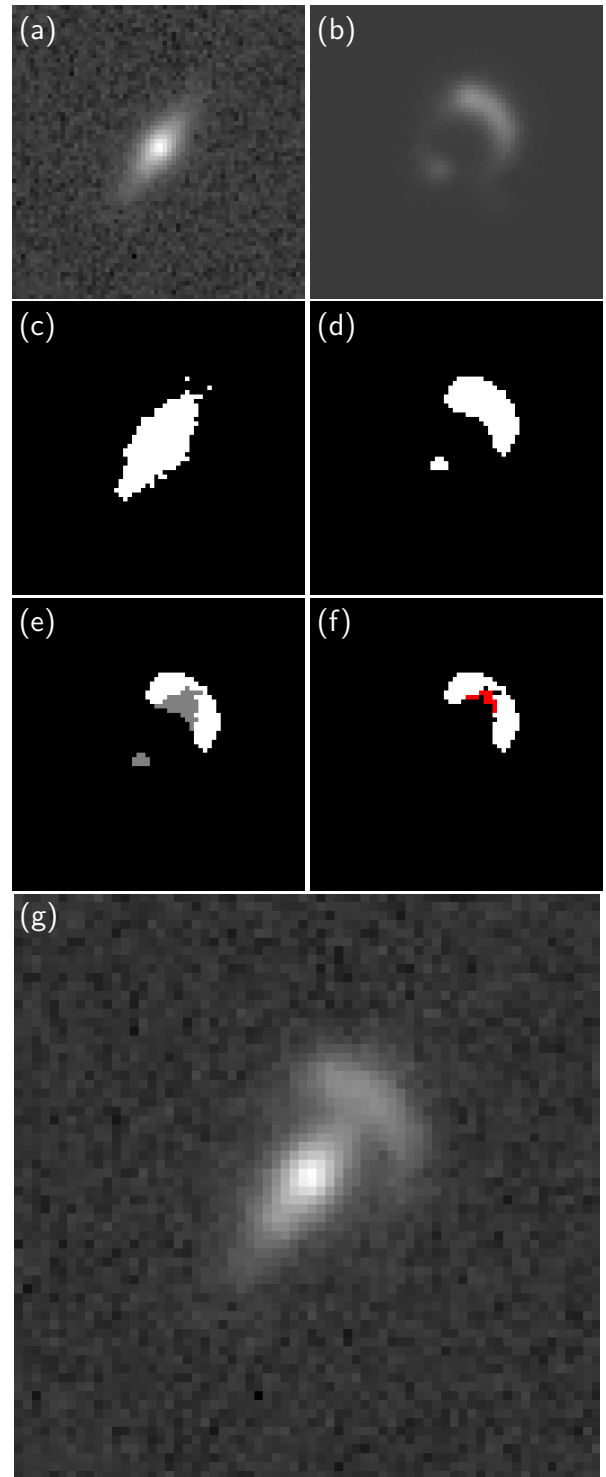


Fig. A.1. Illustration of the contrast check for mock lenses. *Panels (a) and (b)* present the deflector and lensed source light, respectively. *Panels (c) and (d)* show the activated pixels of the deflector and lensed source, respectively. *Panel (e)* presents the activated pixels of the source, but highlighting in grey the pixels that overlap with the deflector mask. *Panel (f)* shows all the pixels dominated by the lensed source light, which are used to decide if the mock passes the contrast check. Among them, we highlight in red the pixels that overlap with the deflector, but are still dominated by the lensed source. Lastly, *panel (g)* shows the final mock lens, which passes the contrast check.

Appendix B: Examples of mock lenses

We present in Fig. B.1 examples of the mock lenses that we use to train the CNN. They are grouped by Einstein radius and generated following the methodology described in Sect. 4.

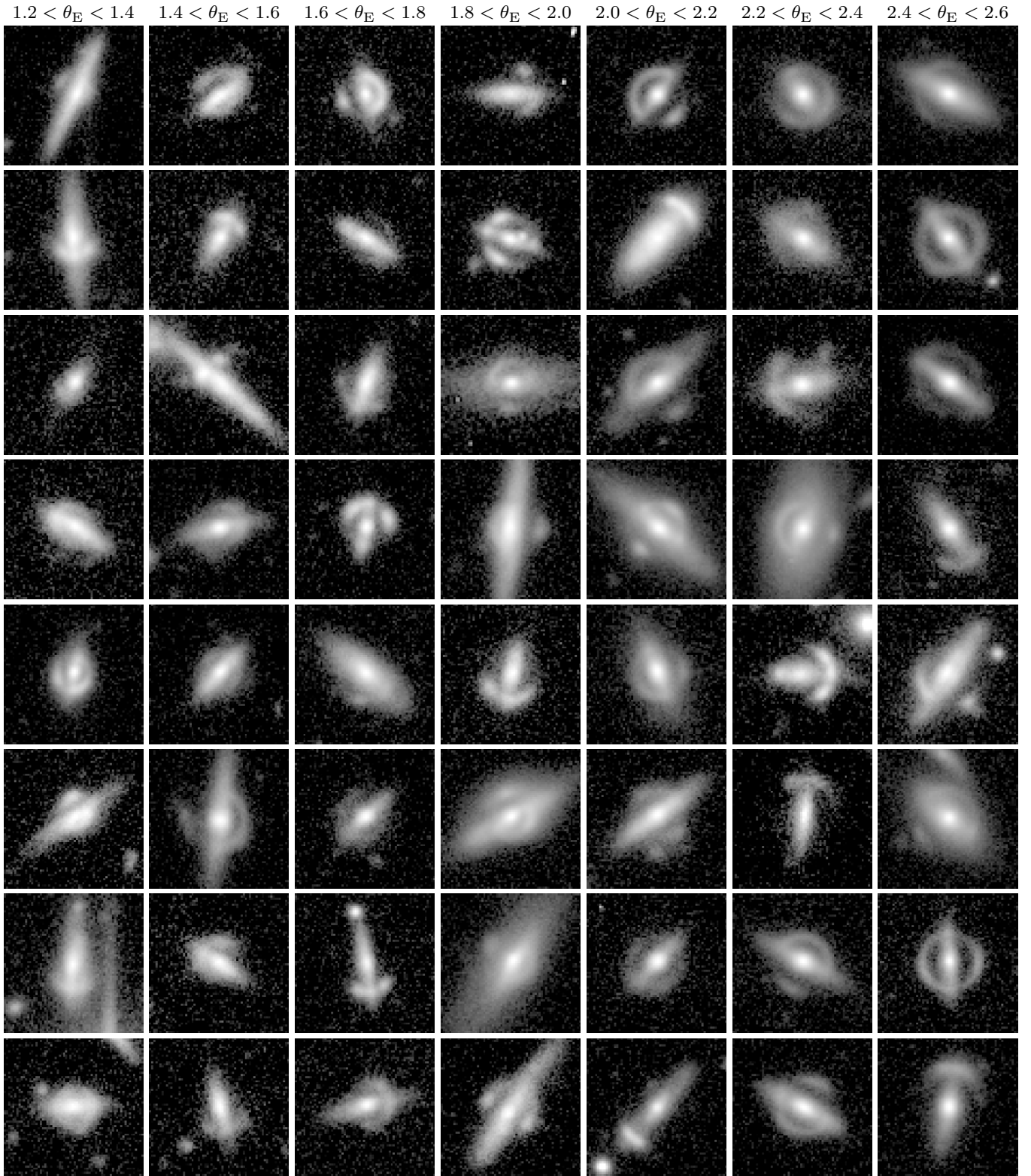


Fig. B.1. Mosaic of simulated edge-on lenses mimicking UNIONS r -band observations. They follow the prescriptions of Sect. 4 and are sorted left-to-right by Einstein radius. Each image is $12''256 \times 12''256$ in size, corresponding to 66×66 pixels.

Appendix C: Table of edge-on lens candidates

Table C.1. List of edge-on lens candidates. The columns correspond to the IAU name of the lens, right ascension, declination, UNIONS u - and r -band photometry using SExtractor's keyword MAG_AUTO, the visual inspection grade, and reference to the earliest discovery paper for the previously reported candidates.

Name	RA	Dec	AB magnitude		Grade	Reference
			u	r		
J0022+3320	5.7309436	33.3474960		19.9696 ± 0.0070	A	
J0142+3057	25.5424303	30.9605795		18.1876 ± 0.0020	A	
J1042+4320	160.7169116	43.3421165		19.2626 ± 0.0053	A	
J1505+5808	226.3265620	58.1382142		19.7085 ± 0.0050	A	
J1559+3147	239.8472065	31.7867967	19.9230 ± 0.0249	17.0137 ± 0.0011	A	Cañameras et al. (2020)
J0120+3345	20.1788702	33.7662481		18.6669 ± 0.0029	B	
J0726+7219	111.7042515	72.3261701		18.7084 ± 0.0029	B	
J0757+4301	119.4758030	43.0255586		19.8280 ± 0.0052	B	
J0758+3020	119.6932428	30.3345799	22.5128 ± 0.0925	19.7480 ± 0.0081	B	
J0811+4339	122.8543425	43.6600055		19.5493 ± 0.0079	B	
J0836+4817	129.1509474	48.2978828		18.8316 ± 0.0042	B	
J0857+3900	134.2974125	39.0126772	20.6838 ± 0.0317	17.9815 ± 0.0015	B	
J1051+2941	162.8862229	29.6973580	20.6246 ± 0.0229	18.4459 ± 0.0021	B	
J1115+3117	168.7664931	31.2907919		20.2914 ± 0.0119	B	
J1121+4351	170.4394276	43.8543797	20.3017 ± 0.0210	17.7539 ± 0.0011	B	
J1152+3507	178.1576661	35.1238394		18.3464 ± 0.0026	B	
J1214+4344	183.5592272	43.7499409		17.3485 ± 0.0018	B	
J1302+4100	195.7132585	41.0023680	22.1846 ± 0.0832	19.0674 ± 0.0044	B	
J1345+4906	206.4890961	49.1027004		19.0217 ± 0.0043	B	
J1356+5321	209.1775710	53.3648699		18.1411 ± 0.0015	B	
J1447+6259	221.8319148	62.9958523		19.3748 ± 0.0055	B	
J1629+4007	247.3489451	40.1202681		17.6530 ± 0.0015	B	
J1649+3202	252.3744709	32.0443551		19.6518 ± 0.0085	B	
J1702+3359	255.6542281	33.9981627		17.3697 ± 0.0014	B	
J1719+3702	259.8905539	37.0369870	19.9697 ± 0.0158	17.4750 ± 0.0012	B	
J0043+3018	10.9464822	30.3134246	20.6487 ± 0.0220	17.4554 ± 0.0010	C	
J0122+3606	20.6597358	36.1056220	21.8596 ± 0.0576	18.1865 ± 0.0019	C	
J0151+3310	27.7945794	33.1739183	20.0504 ± 0.0289	17.6152 ± 0.0017	C	
J0153+3440	28.2903244	34.6712015	21.4819 ± 0.0383	18.2097 ± 0.0016	C	
J0702+7025	105.6683506	70.4204100		17.3727 ± 0.0012	C	
J0730+4144	112.5626555	41.7479087	20.4375 ± 0.0230	17.4948 ± 0.0018	C	
J0743+4613	115.8307597	46.2167520	22.1459 ± 0.0970	19.0604 ± 0.0032	C	
J0806+5434	121.5190539	54.5745299		19.3298 ± 0.0067	C	
J0812+4242	123.2002022	42.7094191		18.6894 ± 0.0024	C	
J0817+5329	124.4889815	53.4859594		18.8634 ± 0.0032	C	
J0819+4515	124.8501970	45.2612734	21.6504 ± 0.0742	18.5855 ± 0.0023	C	
J0821+3239	125.4266641	32.6653315	21.7090 ± 0.0267	18.6794 ± 0.0029	C	
J0827+3021	126.7561980	30.3640160	20.9866 ± 0.0238	19.0879 ± 0.0052	C	
J0829+3122	127.3464117	31.3751107	21.3560 ± 0.0391	18.6363 ± 0.0025	C	
J0853+7533	133.3933297	75.5503074		17.5901 ± 0.0012	C	
J0906+3826	136.5693640	38.4449654	20.0541 ± 0.0230	17.1936 ± 0.0016	C	
J0917+3710	139.2859126	37.1777426	19.4074 ± 0.0142	17.0843 ± 0.0011	C	
J0926+4112	141.6601598	41.2050782	20.4083 ± 0.0339	17.5684 ± 0.0012	C	
J0946+4034	146.7364754	40.5765770	20.5413 ± 0.0254	17.9336 ± 0.0022	C	
J0953+3324	148.4888058	33.4095008	21.0903 ± 0.0204	18.0557 ± 0.0016	C	
J1008+4328	152.0535841	43.4761871		18.7321 ± 0.0028	C	
J1021+4425	155.3771910	44.4282434		19.0770 ± 0.0036	C	
J1024+4916	156.1962473	49.2686515		17.4974 ± 0.0011	C	
J1042+3131	160.5660592	31.5225667		18.2438 ± 0.0021	C	
J1045+3830	161.4509561	38.5006307		19.4541 ± 0.0057	C	
J1048+3412	162.1691522	34.2107643	19.8473 ± 0.0116	17.6184 ± 0.0012	C	
J1049+4407	162.3353987	44.1247252	20.3411 ± 0.0433	18.2829 ± 0.0019	C	
J1055+4508	163.7578525	45.1374880		19.7559 ± 0.0069	C	
J1109+3803	167.4941749	38.0611842		18.1739 ± 0.0024	C	
J1121+3849	170.3750043	38.8255148		19.2811 ± 0.0057	C	

Table C.1. continued.

Name	RA	Dec	AB magnitude		Grade	Reference
			u	r		
J1219+3043	184.8306531	30.7172617	20.9759 ± 0.0326	18.1057 ± 0.0023	C	
J1240+3611	190.1166129	36.1972463	23.8831 ± 0.2015	19.9300 ± 0.0073	C	
J1256+3620	194.0349729	36.3414725	21.2798 ± 0.0559	18.5258 ± 0.0035	C	
J1309+3029	197.2601059	30.4984685		19.3998 ± 0.0048	C	
J1311+4608	197.8431059	46.1435622		17.1290 ± 0.0012	C	
J1317+3602	199.4890447	36.0437890	21.6519 ± 0.0653	18.3090 ± 0.0021	C	
J1350+5515	207.5600484	55.2558622		17.9206 ± 0.0019	C	
J1352+3013	208.0503035	30.2278242		18.5916 ± 0.0041	C	
J1357+4934	209.4420116	49.5728381		17.4802 ± 0.0010	C	
J1406+5753	211.5312925	57.8922726		18.5163 ± 0.0028	C	
J1406+3029	211.7483549	30.4885433	21.3309 ± 0.0480	18.3893 ± 0.0022	C	
J1442+4228	220.7377880	42.4693250	20.9111 ± 0.0588	18.2496 ± 0.0024	C	
J1517+6233	229.4642549	62.5608722		19.1234 ± 0.0036	C	
J1518+3516	229.5567630	35.2735776	21.3932 ± 0.0417	18.3529 ± 0.0021	C	
J1549+4345	237.3001026	43.7656831		18.5109 ± 0.0022	C	Shu et al. (2022)
J1622+5330	245.7261661	53.5040794		18.9184 ± 0.0037	C	
J1623+5448	245.9817018	54.8155471		19.1424 ± 0.0050	C	
J1632+3611	248.2265743	36.1840358		18.9877 ± 0.0035	C	
J1642+5611	250.5932047	56.1881179		20.0957 ± 0.0076	C	
J1644+4719	251.1189270	47.3251309		19.4637 ± 0.0040	C	
J1659+6004	254.7637000	60.0771028		19.2814 ± 0.0040	C	
J1710+3247	257.5724374	32.7922491		17.8119 ± 0.0018	C	
J1715+4459	258.8319945	44.9888158	21.5969 ± 0.0747	18.1896 ± 0.0019	C	
J1730+3305	262.7135754	33.0914681	20.5849 ± 0.0467	17.6751 ± 0.0016	C	
J1751+4028	267.8865464	40.4761924	21.2297 ± 0.0298	19.2625 ± 0.0043	C	
J1818+5736	274.7122803	57.6039647	20.9636 ± 0.0822	17.8255 ± 0.0014	C	
J2324+3143	351.0431226	31.7173002	22.4031 ± 0.1010	18.7777 ± 0.0033	C	
J2346+2952	356.5326571	29.8685802		18.4314 ± 0.0032	C	
J2359+2940	359.8239254	29.6824149	22.1160 ± 0.0511	19.0125 ± 0.0042	C	

Appendix D: Table of other lens candidates**Table D.1.** List of non-edge-on lens candidates. Same layout as Table C.1.

Name	RA	Dec	AB magnitude		Grade	Reference
			u	r		
J0030+3525	7.5491985	35.4193203		20.3806 ± 0.0145	A	
J0147+3540	26.7805603	35.6831946	20.8428 ± 0.0513	19.4105 ± 0.0061	A	
J0727+4938	111.9786573	49.6463066	21.5481 ± 0.0983	20.4514 ± 0.0157	A	Stein et al. (2022)
J0744+4511	116.1995056	45.1903467	20.9530 ± 0.0288	18.8995 ± 0.0022	A	
J0830+3900	127.5749841	39.0054697		18.3616 ± 0.0028	A	
J0847+4316	131.9812843	43.2683410	22.8081 ± 0.0539	19.9818 ± 0.0080	A	
J0854+3424	133.5448406	34.4042774	23.5610 ± 0.1858	18.2880 ± 0.0033	A	
J0854+4817	133.5597432	48.2863870		19.6335 ± 0.0083	A	
J0907+4233	136.8674109	42.5504218		18.5381 ± 0.0038	A	Talbot et al. (2021)
J0917+4104	139.2739719	41.0831402		20.2640 ± 0.0132	A	
J0938+3159	144.5184600	31.9889795		20.4714 ± 0.0100	A	
J0953+4728	148.4602610	47.4674796		20.1084 ± 0.0116	A	
J0958+4021	149.5197456	40.3510648		19.8450 ± 0.0090	A	
J1001+3545	150.3782955	35.7634436		20.2432 ± 0.0087	A	
J1014+5044	153.6731083	50.7475299		19.3181 ± 0.0045	A	Savary et al. (2022)
J1044+3114	161.1144384	31.2343540		20.4778 ± 0.0172	A	Huang et al. (2021)
J1111+4329	167.9780720	43.4863144		20.0567 ± 0.0112	A	Cañameras et al. (2020)
J1121+3657	170.4254175	36.9636376		19.2478 ± 0.0039	A	Huang et al. (2021)
J1210+2942	182.5115475	29.7135649		20.1377 ± 0.0099	A	Stein et al. (2022)
J1240+4509	190.1345492	45.1507984		18.5438 ± 0.0028	A	Huang et al. (2021)
J1433+6007	218.3455098	60.1208466		19.7404 ± 0.0042	A	He et al. (2023)
J1447+4946	221.9233871	49.7742633		19.9587 ± 0.0085	A	
J1527+3718	231.8380701	37.3064436		19.4510 ± 0.0041	A	
J1541+4050	235.4555489	40.8415821		19.3400 ± 0.0047	A	
J1555+4151	238.8239469	41.8606742		19.7357 ± 0.0075	A	Chan et al. (2020)
J1630+4511	247.5053897	45.1981458		18.3119 ± 0.0022	A	
J1635+5108	248.8455393	51.1414327		18.7642 ± 0.0039	A	Savary et al. (2022)
J1641+6612	250.4827149	66.2102977		19.7497 ± 0.0114	A	Huang et al. (2021)
J1652+5505	253.0912792	55.0867535		18.1866 ± 0.0033	A	Huang et al. (2021)
J1655+5957	253.7973159	59.9533299		18.5849 ± 0.0049	A	Storfer et al. (2024)
J0028+3028	7.1125112	30.4731739		17.2964 ± 0.0012	B	
J0137+3508	24.3486937	35.1433615		19.8382 ± 0.0071	B	
J0142+3506	25.7155714	35.1011749		20.3343 ± 0.0133	B	
J0735+4423	113.9150997	44.3876939	21.0947 ± 0.0353	17.6047 ± 0.0019	B	
J0754+7139	118.6354358	71.6619553		19.5501 ± 0.0031	B	
J0840+5136	130.0600175	51.6032234		17.0019 ± 0.0053	B	
J0851+3601	132.8226278	36.0176713		19.8241 ± 0.0064	B	
J0855+3452	133.9534570	34.8735616		17.6041 ± 0.0029	B	
J1313+3155	198.3625467	31.9243948	19.6699 ± 0.0266	18.8308 ± 0.0039	B	
J1403+4619	210.9584120	46.3168808		19.8105 ± 0.0058	B	
J1441+6010	220.3747148	60.1690714		19.3993 ± 0.0050	B	Savary et al. (2022)
J1448+6356	222.1983340	63.9471246		19.0072 ± 0.0043	B	
J1459+4848	224.7911651	48.8096215		19.5763 ± 0.0038	B	
J1529+4329	232.2841803	43.4946833		20.1853 ± 0.0089	B	
J1612+4206	243.0380667	42.1025568		18.9855 ± 0.0018	B	
J1639+4343	249.8090159	43.7222776		17.7454 ± 0.0022	B	
J1735+4731	263.8469395	47.5311135		19.3923 ± 0.0052	B	
J0048+3228	12.0166529	32.4692366	21.4121 ± 0.0565	19.2527 ± 0.0042	C	
J0054+3711	13.6687485	37.1888533	20.7709 ± 0.0189	19.8780 ± 0.0071	C	
J0056+3657	14.0748992	36.9593161		20.3934 ± 0.0063	C	
J0112+3610	18.0914059	36.1756703	21.3250 ± 0.0322	17.7897 ± 0.0018	C	
J0748+7221	117.0648816	72.3561588		20.0681 ± 0.0088	C	
J0749+7245	117.2753637	72.7594174		17.9379 ± 0.0027	C	
J0752+4531	118.1950528	45.5174098	22.9560 ± 0.1159	18.9520 ± 0.0044	C	
J1052+4708	163.0101111	47.1403602	21.7768 ± 0.0623	18.8935 ± 0.0046	C	
J1110+4322	167.5611025	43.3815384	20.2442 ± 0.0314	17.2265 ± 0.0016	C	
J1429+6150	217.4545291	61.8346887		17.4611 ± 0.0021	C	

Table D.1. continued.

Name	RA	Dec	AB magnitude		Grade	Reference
			<i>u</i>	<i>r</i>		
J1448+4841	222.0085402	48.6922657		17.9996 ± 0.0035	C	
J1449+5309	222.3743098	53.1647651		18.7549 ± 0.0035	C	
J1529+3552	232.2822036	35.8812584		20.1486 ± 0.0079	C	
J1707+4929	256.8857557	49.4992241	19.2383 ± 0.0079	17.2830 ± 0.0010	C	
J1716+3257	259.0916613	32.9618078		18.9359 ± 0.0096	C	
J1723+4139	260.8522155	41.6502224	23.1770 ± 0.1764	20.2524 ± 0.0065	C	
J1752+4631	268.0390198	46.5250711	18.7596 ± 0.0033	17.0097 ± 0.0007	C	
J1813+4418	273.4938738	44.3055507		20.1083 ± 0.0142	C	